Modeling Tides and Storm Surge Under Varying Sea Ice Conditions in the Gulf of Alaska and Bering, Chukchi, and Beaufort Seas

Brian Joyce* and Joannes J. Westerink and William Pringle and Damrongsak Wirasaet

Department of Civil and Environmental Engineering and Earth Sciences, University of Notre Dame, Notre Dame, IN

Andre Van der Westhuysen and Robert Grumbine

IMSG at NWS/NCEP/Environmental Modeling Center, National Oceanic and Atmospheric Administration, College Park, MD

Jesse Feyen

Great Lakes Environmental Research Lab, National Oceanic and Atmospheric Administration, Ann Arbor, MI

**Corresponding author address:* Brian Joyce, Department of Civil and Environmental Engineering and Earth Sciences, 302 Cushing Hall, University of Notre Dame, Notre Dame, IN 46556.
E-mail: bjoyce@nd.edu

ABSTRACT

An integrated high resolution tide and storm surge model has been developed for all of coastal Alaska. The model uses the ADCIRC basin-to-channel scale unstructured grid circulation code. Tidal forcing from global tidal models and meteorological forcing from the Climate Forecast System Reanalysis are used. The model's tidal solution has been validated at 121 shelf and nearshore stations. The model's skill has been investigated for summer, fall and winter storms. Sea ice has been incorporated through a parameterized wind drag coefficient which modifies the air-sea drag under ice coverage. Three large storms with distinctly different ice coverages were chosen to exhibit the effect of sea ice on the resulting storm surge. The root mean square error does not exceed 20 cm at any station. Forming coastal ice coverage increases coastal water levels, but the peaks are under predicted at the validation stations. Under dense pack ice, an increase in momentum transfer in the marginal sea ice at the shelf break leads to increased coastal water levels despite the decreased wind stress across the shelf pack ice. In highly variable ice fields, results are mixed, as the underlying assumptions about ice movement used to derive the drag parameterization may fail. To improve model performance for coastal water levels, it would be desirable to include the contribution of wave radiation stresses induced in marginal ice zones. Furthermore, including sea ice drift and current speeds explicitly in the air-sea-ice drag formulation would improve the description of momentum transferred to the water column.

1. INTRODUCTION

Coastal Alaska (Figure 1) spans over 54,000 km with highly diverse geography ranging from sharp volcanic relief in the south to low lying deltas and tundra in the west and north. This high latitude region's complex geometry, bathymetry, coastal features, and tides in conjunction with the presence of powerful storms, leaves the Alaskan coast particularly vulnerable to storm surge and storm waves. In the Bering, Chukchi, and Beaufort Seas, sea ice is present for a significant portion of the year and there is strong inter and intra annual variability in the ice coverage (Erikson et al. 2015). The effect of ice as it relates to tides and storm surges is complex and there are significant uncertainties in the details of this interaction.

The tidal range across the four main basins in the Alaska region is varies dramatically. The coast along the Gulf of Alaska exhibits strong basin edge amplification of the tides. The geometry of Cook Inlet in the western Gulf of Alaska provides favorable conditions for local amplification of the semi-diurnal constituents. The major tidal constituents enter the Bering Sea as a progressive wave from the Pacific Ocean through the Aleutian Islands (Kowalik 1999). As the tide moves through the island chain and over the associated undersea mountain range, high currents and associated vertical and lateral eddying through the passes dissipate tidal energy (Foreman et al. 2006). In the Bering Sea, dissipation over the broad and shallow Bering Sea shelf and the reflections caused by the shape of the partially enclosed basin lead to a complex structure for the main tidal constituents. There is relatively little contribution from the Arctic Ocean to tides in the Bering Sea. Overall, the geometric and bathymetric complexity of the region coupled with the importance of geostrophic effects at high latitudes results in complex tidal dynamics with strong spatial variability.

The exceptionally broad and shallow Bering Sea shelf, intricate coastal geometry, low lying topography, and large, energetic storms, make western Alaska especially vulnerable to storm surge. The November 2011 Bering Sea Superstorm is representative of the high impact storms that pass through the region. An extratropical cyclone which developed over the western Pacific Ocean, this storm entered the Bering Sea over the western Aleutian Islands. The storm intensity matched that of a Category 3 hurricane, with a minimum central pressure of 943 mbar, and sustained winds of 35 ms^{-1}. Measured surges reached up to 3 m in portions of Norton Sound. The resulting storm surge damages were recorded in 37 villages and cities (Kinsman and Deraps 2012).

In Alaskan waters, sea ice usually begins forming in November, and can last in the Bering Sea until as late as July. As the ice forms, it covers the entirety of the Beaufort and Chukchi Seas, while extending to the shelf break of the Bering shelf in the south. Storms in Alaska are also stronger during the late autumn and winter months when portions or entire basins are covered in ice (Mesquita et al. 2010). This ice coverage impacts the energy balance of the ocean during a storm. Momentum from the wind may be imparted to the ice through form drag and skin drag instead of directly to the ocean. The ice then transfers this momentum to the ocean through its movement, altering the relationship between wind speed and ocean stresses, and in turn, the resulting storm surge. Depending on the concentration, type, thickness, shape, and many other factors, this relationship varies. Effectively describing the atmosphere's transfer of momentum to the sea under varying ice conditions is key to accurately predicting major storm surge events in Alaskan waters.

In the past four decades, there has been an observed delay in the formation of sea ice in the Bering Sea which has coincided with a 26% per decade decrease in total sea ice cover in the Bering Sea (Erikson et al. 2015). There is some indication that these changes are already having an effect on the severity of storm environment. Ice drift speeds have doubled over the past two

decades (Spreen et al. 2011), effectively increasing the transfer of momentum to the water at the ice-ocean interface. Quantifying the potential effects of these changing ice conditions requires a baseline understanding of the underlying wind-ice-ocean interactions.

The goal of this work was to develop an accurate and robust computational model of the Alaskan coastal long wave hydrodynamics capable of simulating tides and storm surge with particular focus on how varying ice coverages impact storm surge. In order to accurately model these processes throughout the whole region, a high resolution, flexible unstructured mesh is useful. A mesh of this type allows for the model to capture the complexity of the geography and topography of the region as well as the range of important hydrodynamic processes, including where high gradient solutions are expected. Using an unstructured mesh, which allows for local high resolution is the most efficient way to resolve all of these important features in a domain that encompasses all Alaskan waters.

Both data-assimilated barotropic tidal models (Foreman et al. 2006) and baroclinic coupled ocean-ice models (Danielson et al. 2011) have been developed to study tides in the Bering Sea. These previous works highlight the importance of dissipation of tidal energy as the tide flows through the Aleutian Islands. Storm surge modeling efforts have focused on the Beaufort and Chukchi Seas (Kowalik 1984), and Norton Sound (Johnson and Kowalik 1986; Blier et al. 1997; Chapman et al. 2009). These previous models have not fully resolved coastal floodplains or inlets, and used a variety of methods to account for the presence of ice coverage. This prior work has guided the model development presented in this paper.

We validate our model in ice free conditions by simulating tides and a strong summer storm. A parameterization for air-sea-ice interaction is used to simulate three especially strong winter storms under varying ice conditions. This parameterization and the model's success is assessed.

2. MODEL DESCRIPTION

a. ADCIRC Ocean Circulation Model

The Alaska tide and storm surge model described in this paper applies the unstructured grid Advanced Circulation (ADCIRC) code. ADCIRC as implemented in this model solves the depth integrated barotropic shallow water equations in spherical coordinates in a continuous Galerkin finite element framework to compute water surface elevation and currents (Westerink et al. 2008). The model can be applied over the wide range of scales of motion and hydrodynamic processes that exist when computing the flow of water from the deep ocean to the nearshore, and then into coastal estuaries or onto coastal floodplains. ADCIRC's finite element framework is well suited for computing solutions on large unstructured grids.

b. Model Domain Definition and Development

The Alaska model domain (Figure 2) stretches from the north Pacific Ocean to the Arctic Ocean, including the Gulf of Alaska, Bering Sea, Beaufort Sea, and Chukchi Sea. There are two curved open ocean boundaries in the model. The northern boundary is in the Arctic Ocean with a northernmost point of 80°N, and ranges from 190°W in the west to 134°W in the east. The longer southern boundary follows across the northern Pacific Ocean from 204°W in the west to 128°W in the east. The southern extent of this boundary is 39°N. We chose the boundaries to be primarily in deep water and the tidal signal on these deep ocean boundaries are dominated by the major astronomical tidal constituents while nonlinear tidal constituents are minimal.

The land boundaries of the domain is defined by the Russian coastline to the west, and the Alaskan coastline to the east. The minimum resolution of the model is approximately 5 km in the

deep ocean. The resolution increases to under 1 km on the Alaskan shelf, and most coastal areas are represented using finite elements under 500 m.

The eastern boundary in Alaska contains a number of overland regions which are represented in the model. These overland regions include the deltaic system formed by the Yukon and Kuskokwim rivers in the Bering Sea (Figure 3). This feature has been incorporated into the model in extensive detail, with element sizes as small as 25 m. Many of the remaining overland areas of the model are found north of the Bering Strait, and are resolved at minimum grid size of 25 to 50 m. This includes the numerous inlets and lagoons on the Chukchi Sea facing side of the Alaskan coastline and the barrier islands, lagoons, and floodplains of Kotzebue Sound. The grid itself contains 8,060,620 triangular linear elements comprised of 4,055,605 nodes.

Figure 2 highlights the narrow shelves along Alaska's southern and northern coasts, the subsea mountain ridge that seperates the Pacific Ocean from the Bering Sea and the expansive Bering and Chukchi shelves. The Bering and Chukchi shelves are on average 35-40 m deep and the core Bering Strait region is on average 22 m deep. The model bathymetry and topography comes from a variety of sources including ETOPO1 (Amante and Eakins 2009), the International Bathymetric Chart of the Arctic Ocean (Jakobsson et al. 2012), GEBCO (GEBCO 2014), various National Oceanic and Atmospheric Administration (NOAA) produced digital elevation models (Lim et al. 2011b,a; Carignan et al. 2009b; Medley et al. 2009; Carignan et al. 2009a; Taylor et al. 2008) and the SRTM30 bathymetry and elevation data (Becker et al. 2009).

c. Parameterized Dissipative and Dispersive Processes

The ADCIRC model described in this paper applies three parameterizations to include dissipative processes in the momentum equations. Two are incorporated into the bottom stress term as shown below :

$$\tau_{bi} = \left[\frac{n^2 g}{H^{1/3}} \sqrt{U^2 + V^2} + f_I \right] U_i. \tag{1}$$

In this equation, n equals the Manning's roughness coefficient, g equals gravity, H is the total water column depth, U and V are the horizontal depth averaged velocities, and f_I is a frictional coefficient for the purpose of including dissipation caused by baroclinic internal tides. The first term is a parameterized implementation of bottom friction using a spatially varying Manning's roughness coefficient following the work of Bunya et al. (2010). Deepwater and shelf waters are assigned a Manning's n value of 0.025, while back bays, estuaries and lagoons are are assigned a default value of 0.035. Overland values are assigned using land cover data from the National Land Cover Database (NLCD) (Homer et al. 2015) in conjunction with a method developed by Bunya et al. (2010) to convert the NLCD to representative Manning's n values. Figure 4 shows the Manning's n values for the Yukon - Kuskokwim Delta used in the model. The second term, f_I, is a parameterized description of the dissipation of the barotropric tides due to baroclinic internal tides which are not directly simulated in the model. The internal tide linear friction is defined as:

$$f_I = c_{BC} \frac{N_B (\nabla H)^2}{\kappa}, \tag{2}$$

where N_B is the buoyancy frequency value at the ocean bottom, ∇H is the bathymetric gradient, κ is the wavenumber of the first internal mode at the M_2 tide frequency, and c_{BC} is a free parameter set to 1 (Zaron and Egbert 2006). These quantities are considered to be time independent. The buoyancy frequency is calculated using temperature and salinity casts from the World Ocean Database (Boyer et al. 2013). High grid resolution through the Aleutians and in many key embayments together with an accurate advection scheme and the momentum diffusion term directly simulate lateral eddy structure and dissipation. The eddy viscosity coefficient in the diffusion term is set to 2 $m^2 s^{-1}$ in water and 20 $m^2 s^{-1}$ overland.

d. Tidal Forcing

Tides are forced in the model with a periodic elevation boundary condition using the eight dominant astronomical tidal constituents, the semidiurnal M_2, N_2, S_2, K_2 and diurnal O_1, K_1, P_1, Q_1, along the two curved open ocean boundaries. In addition, tidal potential functions and the self attraction and load tide are forced at each node within the model domain for the same eight constituents. The boundary and self attraction and load tide forcing data has been predominantly extracted from Le Provost's FES2012 global tidal model (Carrre et al. 2013). The K_1 constituent boundary forcing was extracted from the OSU TPXO8 global tide model (Egbert et al. 1994; Egbert and Erofeeva 2002). The nodal factors and equilibrium arguments for the tidal forcing are determined based on the starting time and duration of the simulation. A ramping period is used to ensure that any initial transients are minimized prior to times where results are recorded.

e. Atmospheric Forcing

The atmospheric forcing is performed using wind speed and pressure fields produced by the National Centers for Environmental Prediction's Climate Forecast System (CFSv2) (Saha et al. 2014). This model provides hourly wind speeds at a 10 m height with a horizontal resolution of 0.205 degrees by 0.204 degrees, and hourly atmospheric pressure at a resolution of 0.5 degrees. The air-sea drag coefficient, when there is no ice coverage present, is defined by Garratt's drag formula (Garratt 1977) and is limited at 0.0025 in order to represent sheeting of waves at high wind speeds. To propagate low pressure systems into the model domain, the low pressure deficit along the boundary is used to calculate the inverted barometer effect. This is applied to the water surface elevation along the corresponding open ocean boundary.

f. Ice Cover and Forcing

Measurements have shown that the presence of ice cover can lead to changes in the drag coefficient defining the air-sea momentum transfer, which generally has a lower dependency on wind speed at high ice densities (Macklin 1983; Fujisaki et al. 2009). Previous ADCIRC applications in this region (Chapman et al. 2005, 2009) used an approach derived from Birnbaum and Lüpkes (2002) and Garbrecht et al. (2002) to compute a C_{d-ice} to apply as a lower limit on the Garratt drag coefficient.

We sought to use a drag coefficient which integrally combines contributions from both the ice covered and ice free portions of a given element. Various investigations have shown that an area weighted approach (Zippel and Thompson 2016; Lüpkes and Birnbaum 2005; Lüpkes et al. 2013) that considers both the form and skin drag over the ice floe (Lüpkes and Birnbaum 2005; Lüpkes et al. 2013; Lu et al. 2011) can be used as a parameterization for the drag coefficient. This leads to the parameterization used for this work :

$$C_{d-total} = (AF)C_{d-is} + (1-AF)C_{d-w} + C_{d-if} \tag{3}$$

where C_{d-is} is the contribution due to ice skin drag represented as a constant, C_{d-w} is the Garratt wind stress as a function of wind speed over the open water area, and C_{d-if} is the form drag contribution from the ice represented as a semi-parabolic function of area fraction of ice coverage, AF. C_{d-w} was limited at a maximum value of 0.0025. C_{d-is} was chosen based on Lüpkes et al. (2012) to have a value of 0.0015. C_{d-if} maintains the maximum value of C_{d-ice} from Chapman et al. (2005, 2009) of 0.0025 at 50% ice coverage, with minimums of 0 at 0 % and 100 % ice coverage. Figure 5 shows the drag coefficient as a function of both AF and wind speed.

At 0% ice coverage, this parameterization is identical to the limited Garratt drag formulation. As AF increases to 50%, the largest enhancement of the drag coefficient occurs, Figure 6. As AF

increases to 100% $C_{d-total}$ approaches the constant value controlled by C_{d-is}. This formulation does not consider other potentially important factors in the computation of the drag coefficient, such as ice floe geometry, melt ponds, ridges, floe separation distance, or atmospheric stratification (Tsamados et al. 2014). Additionally, the presence of ice makes it such that the momentum lost by the air is not necessarily delivered locally to the water; some of the momentum can be transported away by advecting ice floes and some can be dissipated in ice-ice collisions. In this application it is assumed that there is a proportional relationship between the wind speed and the ice drift-ocean current differential speed which generates the horizontal stresses at the ice-ocean interface.

The gridded sea ice concentration fields used in this paper were developed at the National Centers for Environmental Prediction (NCEP) for use in the NCEP Climate Reanalysis Project (Grumbine 1996, 2014). These fields consist of daily sea ice extent and concentration at a 0.0833 degree resolution. All forcing data is linearly interpolated using available time and spatial fields.

3. Tidal Model and Validation

The tides were computed and validated by applying tidal forcing over a 120 day simulation and harmonically analyzing the resulting time history records over the last 90 days. A 30 day hyperbolic tangent ramp function was applied to minimize the generation of transients associated with the cold start (zero response initial conditions). To validate the tidal solutions, 115 NOAA water level tide gauges along the Alaska coastline (NOAA) and 6 International Association for the Physical Sciences of the Oceans (IAPSO) shelf based stations (Smithson 1992) were chosen. The locations of these stations are shown in Figure 1. The modeled water level signal at these stations was harmonically decomposed using 23 tidal constituents and a comparison was made to the tidal constituents derived from observations at each of these stations (Pawlowicz et al. 2002).

The maximum computed tidal water surface elevation is shown in Figure 7. The global harmonic decomposition shows that the dominant tidal constituents in the model domain are the diurnal K_1 and O_1 constituents and the semidiurnal M_2 and N_2 constituents. The modeled amplitude and phases for each of these constituents are found in Figure 8 and Figure 9. The Bering Sea's exceptionally broad shelf and shallow depths lead to a complex system of standing waves and resonance there in both the diurnal and semidiurnal constituents. There are numerous nodal points appearing as full and degenerate amphidromes. The small amplitudes found in the Chukchi and Beaufort Seas are due to the partially closed nature of the Bering Sea, the narrow Bering Strait, and St. Lawrence Island which reflect the dominant tidal wave travelling from the north Pacific Ocean. In addition, the generally smaller tides north of the Bering Strait are due to weakened tidal potential forcing at high latitudes (Westerink et al. 1994).

The amplitudes of the diurnal constituents vary slowly between 0.2 m to 0.5 m in the Gulf of Alaska. In the Bering Sea, the diurnal constituents vary much more rapidly spatially with amplitudes from 0 m to 1 m. There is strong edge amplification along the entire eastern edge of the Bering shelf and especially in Bristol Bay in the southeast Bering Sea. Both of the main diurnal constituents exhibit two prominent amphidromic and one degenerate amphidromic points on the southern portion of the Bering Sea shelf, just north of the Bering Strait, and on the northwestern end of Norton Sound.

The two major semidiurnal constituents have an almost identical structure to each other, with the M_2 constituent being much stronger. Basin edge amplification leads to amplitudes of greater than 1 m for the M_2 tide along the Gulf of Alaska coast. Resonance in Cook Inlet leads to strong amplification of the semidiurnal tide there. The Aleutian Islands have a strong effect on the structure of the semidiurnal tides with large gradients in both amplitude and phase across the island chain. Large gradients are also seen in the Bering Sea with strong amplification in Bristol Bay.

Both semidiurnal constituents have 8 amphidromic points in the domain, with five being located on the Bering/Chukchi shelf. The partially closed nature of the Bering Sea, which reflects the tide and the breadth and depth of the shallow shelf are the main factors contributing to the complexity of the tide in this area. The high level of spatial complexity is more evident in the semidiurnal constituents because of the shorter semidiurnal wavelengths. The amphidromic system in Norton Sound leads to small semidiurnal tidal amplitudes there.

Table 1 shows the modeled to observed difference statistics for the four main tidal constituents at the NOAA and IAPSO stations. Figure 10 summarizes the modeled to observed comparison for the four main tidal constituents and Figure 11 shows the geographic distribution of stations and their corresponding error. The coefficient of determination, or R^2 values, for the computed amplitudes of the main diurnal constituents range between 0.845 and 0.962, while the R^2 values for the diurnal phases range between 0.902 and 0.956. The absolute average error for each of the constituents is 3.5 cm and 2.5 cm respectively for the K_1 and O_1 constituents respectively. The largest sources of error for the amplitudes of the diurnal constituents are found at the stations up the Kuskokwim River and in Norton Sound. The model may include an inaccurate description of certain features in the Kuskokwim River. The bathymetry is notably difficult to measure with high resolution methods, such as LIDAR, due to turbidity in the water. Additionally, no river inflow is included in the model. The stations with the largest errors in Norton Sound, such as Unalakleet and Shaktoolik, are found within or in front of inlets and back bays which have not been fully resolved in the model. These inlets and other details are important for capturing localized gradients in the tidal amplitudes due to dissipation as the tide propagates into the backbay. In addition, the location of a degenerate amphidrome in the westernmost portion of Norton Sound increases the challenge of modeling the diurnal tide at these stations. There is also a concentrated error near the amphidromic point north of the Bering Strait found in both diurnal constituents. This is particularly evident in the K_1

constituent modeled phases in the eastern Chukchi Sea. The computed phases are approximately 100 degrees out of phase with the observed phases at these stations. This error is likely associated with an incorrect location of the amphidromic point in the diurnal constituents north of the Bering Strait. This could be attributed to inaccurate representations of the shelf edge or bottom friction as amphidromic points can be strongly impacted by the frictional dynamics (Rienecker and Teubner 1980). In addition the elevation forced tidal boundary conditions on the northern boundary for the diurnal constituents differed greatly between global tidal models and may be a source of error.

The semidiurnal tide is generally well predicted with R^2 values of greater than 0.947 for all amplitudes and greater than 0.953 for the phases. The absolute average error is 8 cm for the M_2 tide. The phase comparisons show excellent agreement, especially in the vicinity of amphidromic points in the Bering Sea. Prior to the addition of parameterized internal tide dissipation to the model, the M_2 amplitude was overpredicted by at least 20% at each of the tidal stations found on the north side of the Aleutian Islands. The Aleutian Islands and related strong bathymetric gradients are conductive to generating internal tides that dissipate the barotropic tide as parameterized by Equation 2. Moreover, the tidal currents tend to be strong in the area (see Figure 12), also leading to greater dissipation. Inclusion of this parameterized baroclinically generated dissipation effectively halved the average error in the semidiurnal amplitudes on the north side of the Aleutians.

Of the 121 validation stations, only 20 stations used a timeseries greater than 3 months to derive the harmonic constituents. A longer record would be desirable to improve the accuracy of the harmonic decomposition. The simulations presented in this paper do not include the effects of sea ice dissipation on the tide. Many of the comparison constituents are based on ice free records as most of the stations throughout western and northern Alaska are short term and were deployed in ice free conditions. However we do anticipate an effect of intra-seasonal variability as large

portions of the Bering and Chukchi Sea are covered in ice year round. This would particularly impact the tide propagating from the northern boundary of the model. Meteorology is also ignored in this tidal validation and may affect total dissipation and/or may drive pressure modes on the regional and basin scale.

4. STORM SURGE UNDER ICE FREE CONDITIONS

To validate the coupled tide and storm surge model, the model was run for August 2012, an ice free summer month with a major storm event along the coast of western Alaska. Summer storms in the region are typically longer, less intense, and slower than storms in late fall and winter (Mesquita et al. 2010) with lower mean storm surge heights. This month was simulated using a 16 day ramping period and a 31 day simulation with tidal forcing and the hourly CFSv2 atmospheric forcing applied. This simulation was also run without tidal forcing in order to better understand the evolution of storm surges. All three NOAA stations with data were used to validate the computed water levels along the coast of western Alaska; Nome, Red Dog Dock and Prudhoe Bay. Nome is located at the head of Norton Sound, Red Dog Dock sits on the Chukchi Sea to the north of Kotzebue Sound, and Prudhoe Bay is located in the north of Alaska on the Beaufort Sea, Figure 1.

The simulation was performed with a focus on August 14th to 18th, 2012. The event of interest consisted of predominately southerly winds, moving from west to east over the Bering Sea and led to increased water levels over a large portion of the coastline, both north and south of the Bering Strait. Figure 13 shows the progression of the storm's wind and pressure field and the development of storm surge. In general, the storm surge component of total water level is focused on the shelves and sounds and amplifies along the eastern shores of the Bering and Chukchi Seas. As the storm moved over Norton Sound in the morning of the 15th, over 1 m of surge was built

up along the northern portion of the Sound. The surge entering Norton Sound was amplified in the eastern portion of the sound, particularly Norton Bay, and held against the northern portion by strong winds. The storm produced strong mainly southerly currents of up to 1 ms^{-1} within the Bering and Chukchi Seas and through the Bering Strait. The modeled elevation and current fields are strongly impacted by geostrophic effects, particularly in the west of Norton Sound and along the North Slope where storm surge is increased by up to 0.3 m due to geostrophic effects.

The CFSv2 forcing matches the observed meteorology closely at all stations, shown in Figure 14. Figure 15 shows that the water surface elevation response at all stations is well captured. Table 2 shows that the peak errors and root mean square error of the water surface elevation response are small. The peak error at any of the stations is no more than 6.7 cm.

5. STORM SURGE IN THE PRESENCE OF ICE COVERAGE

In the winter and late fall, there are a higher number of extreme events in the Alaska region (Mesquita et al. 2010). Storms representative of this trend affected the Bering Sea in November 2011, February 2011 and January 2017. Figure 16 shows the area fraction (AF) of ice, or percent ice coverage over the model domain during November 2011, February 2011 and January 2017. The November 2011 storm occurred while narrow marginal ice zones were starting to form along the coasts of the Chukchi and Bering Seas with partial 50% area fractions being representative. In this model, sea ice in these concentrations increases the amount of momentum imparted into the sea under wind forcing. In February, the Chukchi Sea and most of the Bering Sea north of the shelf break was covered in pack ice with an area fraction between 95% and 100%. An ice coverage greater than 90%, specifically in strong winds, is capable of decreasing the wind stress on the water. The zone adjacent to the shelf break was covered in an extensive marginal ice zone with highly variable AF ice. Due to a low Arctic sea ice extent in January 2017, much of the ice

in the Bering Sea was present in concentrations ranging from 30% near the ice edge to 70% closer to shore. Again, when considering the ice based drag parameterization used in this work, these ice concentrations represent the range with the greatest possibility for the enhancement of air-sea momentum transfer.

All three storms were of similar strengths, with similar tracks, and resulted in over 2 m of surge in western Alaska. Each of the storms were simulated as part of a month long simulation with and without tides. A five day ramping period was used for tides. To quantify the impact that ice coverage had on the resulting surge, each storm was also run without considering ice coverage.

a. November 2011

This extratropical cyclone affected the Bering Sea and coastal Alaska from November 8th to November 11th, 2011. The storm entered the model domain late into the day on November 7th with a central low pressure of 943 mbar, with a track over the western Aleutian Islands and a cohesive cyclonic structure and maximum sustained wind speeds reaching 35 ms^{-1}. The progression of the storm in the Bering Sea and the response in water surface elevation without tides are shown in Figure 17. As the storm moved over the Bering Sea shelf, strong shelf currents in excess of 2 ms^{-1} developed. The predominantly southerly and southeasterly winds, forced water into and across Norton Sound with strong cross-sound setup and through the Bering Strait. Late in the day on November 9th, the storm clearly separates into two bands. As the first band of strong southeasterly winds passed, storm surge was built up in the eastern and northern portion of Norton Sound, and amplified in Norton Bay. This band maintained its strength north of the Bering Strait, causing storm surge to build up along the coastal areas northeast of the Bering Strait, including Kotzebue Sound and at Red Dog Dock. In between these two bands, calmer winds allowed for the storm surge to relax and begin to exit Norton Sound. However as the second, slightly weaker, band of

westerly winds moved over Norton Sound surge was again built up in the eastern and northern portion. This second band had weakened significantly travelling north and therefore had much less effect on water levels north of the Bering Strait.

Figure 18 shows that the CFSv2 meteorology at Nome, Red Dog Dock and Prudhoe Bay captures most of the details of the wind speed and atmospheric pressure. The water surface elevation comparisons throughout the month long period at these same stations are generally good, with the exception of the peaks associated with the strongest portion of the storm, Figure 19. An analysis of the peak errors at each station for the winter storms is shown in Table 3. The initial storm surge peak at Nome on November 9 around 10:00 GMT is underpredicted by 0.43 m when not considering ice coverage. Considering ice coverage enhances the surge, matching the peak within 0.02 m, a significant improvement. The first peak at Red Dog Dock on November 10 around 2:00 GMT of 1.67 m is underpredicted by 0.53 m, despite a 0.15 m increase when adopting the ice drag law. The ultimate peak surge on November 10 of 2.7 m at Nome is underpredicted by 0.89 m despite an increase in the modeled signal due to ice coverage of approximately 0.3 m. The second smaller peak at Red Dog Dock of 0.5 m is accurately captured with an approximate 0.1 m increase once again due to ice. The increase in water levels due to ice is focused at the coast, particularly along the near shore marginal ice zone in Norton Sound where winds were strong, Figure 20. We also note that the post event drawdown on November 13 at Red Dog Dock is over-predicted by 0.49 m when considering ice while correctly modeled without ice. Table 2 shows that considering ice coverage improves the overall accuracy of the peak water surface elevation responses while achieving a similar root mean square error.

The under prediction of the two peak surges can be attributed to a variety of possible processes. There is clearly some under prediction of the CFSv2 wind speed at both Nome and Red Dog Dock associated with the different bands of the storm. This may be due to a low bias in the wind forcing

or the low resolution of the CFSv2 model compared to the ADCIRC model. Measured significant wave heights reached 12 m in the Bering Sea on November 9th (Kinsman and Deraps 2012). As these waves move onto the shelf and transform due to depth limited breaking and within the shore marginal ice zone as it existed, the resulting wave radiation stress gradients will add significant shore directed forcing in the shallow nearshore zone. Given the shallow bathymetry this effect can increase water levels by as much as 0.5 m to 1 m in ice free conditions (Dietrich et al. 2010, 2011, 2012). Coupling to a phase-averaged wave model that includes the effect of ice on waves would allow for wave momentum, input over much of the Bering Sea, to be transferred to the surge over the relatively narrow coastal ice zone. Additionally, the degree to which uncertainty in the air-sea-ice interaction as implemented limits the accuracy of the current model is unclear. The underlying assumption of a high correlation between ice drift speed (relative to the water currents) and wind velocity may be violated under the marginal ice and extreme wind conditions. In particular, the drawdown event at Red Dog Dock suggests over-prediction when ice effects are considered, possibly because ice may be drifting out of Kotzebue Sound with the surge recession and therefore violating the underlying speed and velocity relation assumption.

b. February 2011

The major February 2011 storm event affected the Bering Sea region from the 22nd until the 25th, following two slightly weaker storms. This storm had a similar track to the November 2011 storm, but weakened much farther south over the Bering Sea. The minimum central pressure of the storm reached 955 mbar in the domain, and the strongest winds exceeded 30 ms^{-1}. Storm surge was built up on the eastern edge of the Bering Sea basin and amplified greatly on the shelf. Blocking by St. Lawrence Island directed surge into Norton Sound, although some was also forced to the northwest between the island and the Chukotka Peninsula and eventually through the

Bering Strait. Because the wind speeds over the shelf were much weaker than in November, the shelf velocities generated during the storm on the Bering shelf were weaker in comparison. The storm surge directed into Norton Sound was amplified in the eastern and northern portion. A high pressure system measuring greater than 1050 mbar followed the storm inducing a negative surge. The progression of the wind and pressure fields and the development of water levels through the storm are found in Figure 21.

Once again, while the wind direction and pressure of the CFSv2 model matched observations closely, Figure 22, there is a clear under representation of the storm's wind speed at Red Dog Dock. The comparisons for water surface elevation throughout the month long period are generally very good, Figure 23. The successive storms produce peak surges which are shown in Table 3). Peak water levels for the surge events for the first and third surges are underpredicted by 0.1 to 0.3 m, although accounting for ice in the air-sea interaction formula enhances surges by up to 0.1 m and brings all peaks into better agreement with the measurements. The second peak at both Nome and Red Dock Dog are predicted accurately and indicate little effect of ice.

The February ice coverage generally leads to a slight increase in total water levels at the validation stations. The drag law applied controls the drag coefficient for stronger winds over the shelf to be between 0% and 20% less for these storms, suggesting we would see a reduction in storm surge instead of the increase seen. Computing the difference in computed maximum water levels with and without ice effects, Figure 20, suggests that a 0.2 to 0.4 m lift across the entire Bering shelf is driven by the significant enhancement of air-sea drag in the broad marginal ice zone that spans across the Bering Sea shelf break. The air-sea drag law applied increases the drag coefficient by up to 200% for the wide range of ice concentrations that occur in the marginal ice zone. The addition of ice coverage generally improves the overall accuracy for this storm and the peak errors, Table 2.

Two possibly important processes are still are missing in these simulations. We are not considering momentum imparted to the sea through wave dissipation, particularly in the marginal ice that stretches across the Bering Sea at the pack ice/ice-free water interface. Additionally, any damping of storm surge and tidally driven currents which may occur under the dense pack ice is not considered. Overall, the dense ice pack case is well modeled and it is clear that far from providing a protective cover from storm surge over the ocean during winter, high concentrations of pack ice allow for significant surge events along the western Alaskan coast.

c. January 2017

In January 2017, a series of low pressure systems with strong winds followed an extratropical cyclone with a central low under 940 mbar, again on a similar track to both the February and November 2011 storms. Winds were again predominantly southerly and speeds exceeded 35 ms^{-1}. As the increased water levels propagated into the eastern half of the Bering Sea, they were amplified on the shallower portions of the shelf. This led to 5 days of significantly elevated water levels for the entire northern edge of the Bering Sea and much of western Alaska. The progression of the wind and pressure fields and the development of water levels without tides through the storm are found in Figure 24.

By January 2017, a meteorological and water level gauge had been installed at Unalakleet, in the easternmost portion of Norton Sound. The validation of the CFSv2 meteorology at Nome, Unalakleet, and Red Dog Dock as shown in Figure 25. The computed and measured water levels are shown at Nome, Unalakleet, Red Dock Dock, and Prudhoe Bay in Figure 26. Three to four well defined peaks appear at the western Alaskan stations with maximum surge values shown in Table 3. The comparison between modeled and measured water levels are generally good. In non-peak surge portions of the record, the no-ice simulation better matched the record while the ice

simulations predictions often being either too low or too high. Table 2 shows that the root mean square error at the validation stations is increased by including ice coverage. During the peak water levels, the inclusion of ice over predicts some of the peak water levels, for example, by up to 0.5 m at Nome for portions of the storm, but accurately captures the ultimate peak. Regionally, the presence of ice changes water level by as much as 0.6 m throughout the simulation, Figure 20. This increase is coastally focused in the Bering Sea correlating to the variable ice field there. In the Chukchi Sea, the effect is more regional due to the broader and denser ice coverage there.

Clearly the air-sea-ice momentum transfer parameterization employed in this work imparts too much momentum to the surge in some scenarios. Again, this application assumes that there is a proportional relationship between the wind speed and the ice drift/ocean current differential which generates the horizontal stresses at the ice-ocean interface. This assumption may be particularly flawed in the case of the highly fractured ice fields under strong winds. Additionally, the afore-mentioned ice-wave and wave-surge interactions would have a large effect on this storm surge for this storm events due to the extensive partial ice field.

6. CONCLUSIONS

Our high resolution, tide and storm surge model for Alaska connects all four major basins in the region, the Gulf of Alaska and Bering, Chukchi and Beaufort Seas in order to better model processes across these marginal seas. The model represents, at scales ranging from 5000 m to 25 m, the geometric, bathymetric/topographic and surface roughness complexity of the Alaskan coast. Tidal constituents from global tidal models are used as boundary conditions in order to simulate tides throughout the domain. The Climate Forecast System version 2 reanalysis wind and pressure fields provide atmospheric forcing. NCEP's Automated Sea Ice Analysis fields and a

parameterization of the form and skin drag over the ice allow for the effect of ice to be taken into account when computing storm surge.

The tidal model has been validated at 115 NOAA and 6 IAPSO stations for the 8 dominant astronomical tidal constituents without considering the impact of the meteorology or sea ice. The model accurately represents the complexity of the semi-diurnal constituents in the Bering Sea and the main diurnal tidal constituents are also well represented. The major sources of error are in areas where bathymetric features and river inflows are not fully resolved and at stations located in close proximity to some of the northernmost amphidromic points.

Under ice free conditions, we have simulated the storm surge from a significant summer storm and validated the water elevation response at the three available stations in western and northern Alaska. Given an accurate representation of the meteorology, the model is capable of accurately simulating the development of storm surge generated by summer storms at these stations. For more energetic storms occurring in the presence of ice cover, results are mixed, particularly in the most intense portions of the storms. Some of the under-prediction may be related to localized under-prediction in the CFSv2 winds. It is unclear if this is a near shore transitional effect or extends more broadly over the Bering and Chukchi Seas. The November 2011 storm occurred during a period of forming marginal coastal ice and the response closely matches observations with the exception of the peak surges. With forming ice at around 50% coverage bordering the coast, the with ice model shows a small increase in the simulated peak water level at these locations, improving results as shown in Table 2. However, the peak storm surge generated from this storm is still significantly underpredicted. The inclusion of breaking waves at the coast, particularly through the coastal marginal ice zone, may enhance coastal surge through enhanced wave setup.

Of the winter events simulated, the February 2011 simulation, where the ice field was generally greater than 95% and covered the majority of the Bering Shelf, most closely matches the observed

coastal water levels. Table 2 and the modeled responses suggest that even under a dense pack ice, coastal water levels can be modestly increased due to ice coverage, despite the fact that the air-sea-ice drag relationship suggests a reduction in wind drag under dense ice coverage. This ice enhancement effect was generated by increased momentum transfer in marginal ice fields at the edge of the Bering Shelf which led to increased water levels by approximately 20 cm in the entire eastern half of the Bering Sea, improving the prediction of peak water levels at the coastal stations.

The highly variable ice field present for the January 2017 storm simulation led to the most significant variation of the computed to measured response. Although accounting for ice coverage enhanced and improved the computed surge during some portions of the various storms, in general the response for both peak surges and recession events was better when not considering ice coverage. This suggests the missing complex interplay between wave radiation stress in the nearshore partial ice coverage is important and that wind-ice differential movement that does not always adhere to the assumed correlation in the drag law used in our model.

It is clear that the uncertainty in the applied drag parameterization and the fact that the ice movement does not always correlate to the wind speed as was assumed by our air-sea-drag implementation; the lack of a wave model, especially one which considers ice and the momentum imparted to the water through both depth limited wave breaking and waves breaking in the marginal ice zones; and potential limitations of the meteorological forcing in high energy sections of the storms do not allow for the model to represent the largest storm surges as accurately as with the weaker summer storms. We envision future work focused towards developing a greater understanding of how ice coverage influences tidal and storm surge processes, in order to draw conclusions about the potential dangers or benefits of a changing ice environment as it relates to storm surges. This should include coupling long wave hydrodynamics directly to a phase-averaged wind wave model

which considers sea ice physics, and the direct computation of wind and current induced ice ocean stresses through a coupled sea ice model which computes ice motion.

Acknowledgments. This work was supported by Western Alaska Landscape Conservation Cooperative Project WA2012_14. J.J. Westerink was also supported by the Henry J. Massman and the Joseph and Nona Ahearn endowments at the University of Notre Dame.

References

Amante, C., and B. W. Eakins, 2009: ETOPO1 1 Arc-Minute Global Relief Model: Procedures, Data Sources and Analysis. 19 pp., NOAA Technical Memorandum NESDIS NGDC-24.

Becker, J. J., and Coauthors, 2009: Global bathymetry and elevation data at 30 arc seconds resolution: Srtm30_plus. *Marine Geodesy*, **32 (4)**, 355–371, doi:10.1080/01490410903297766.

Birnbaum, G., and C. Lüpkes, 2002: A new parameterization of surface drag in the marginal sea ice zone. *Tellus A*, **54**, 107–123.

Blier, W., S. Keefe, W. A. Shaffer, and S. C. Kim, 1997: Storm Surges in the Region of Western Alaska. *Monthly Weather Review*, **125 (12)**, 3094–3108, doi:10.1175/1520-0493(1997)125⟨3094:SSITRO⟩2.0.CO;2.

Boyer, T., and Coauthors, 2013: World Ocean Database 2013. 209 pp., NOAA Atlas NESDIS 72, S. Levitus, Ed., A. Mishonov, Technical Ed.; Silver Spring, MD.

Bunya, S., and Coauthors, 2010: A High-Resolution Coupled Riverine Flow, Tide, Wind, Wind Wave, and Storm Surge Model for Southern Louisiana and Mississippi. Part I: Model Development and Validation. *Monthly Weather Review*, **138 (2)**, 345–377, doi:10.1175/2009MWR2906.1.

Carignan, K., T. Sazonova, L. Taylor, B. Eakins, R. Warnken, and D. Schoolcraft, 2009a: Digital Elevation Model of King Cove, Alaska: Procedures, Data Sources and Analysis. U.S. Dept. of Commerce, Boulder, CO, 22 pp., NOAA Technical Memorandum NESDIS NGDC-23.

Carignan, K., L. Taylor, B. Eakins, R. Warnken, P. Medley, and E. Lim, 2009b: Coastal Relief Model of Southern Alaska: Procedures, Data Sources and Analysis. U.S. Dept. of Commerce, Boulder, CO, 29 pp., NOAA Technical Memorandum NESDIS NGDC-31.

Carrre, L., F. Lyard, and M. Cancet, 2013: FES 2012: A New Global Tidal Model taking Advantage of Nearly 20 Years of Altimetry. ESA Communications.

Chapman, R. S., D. Mark, and A. Cialone, 2005: Regional tide and storm-induced water level prediction study for the West Coast Alaska. U.S. Army Engineer Waterways Experiment Station, Vicksburg, MS., Draft Report to POA.

Chapman, R. S., D. Mark, and A. Cialone, 2009: Storm-induced water level prediction study for the Western Coast of Alaska. U.S. Army Engineer Waterways Experiment Station, Vicksburg, MS., Draft Report to POA.

Danielson, S., E. Curchitser, K. Hedstrom, T. Weingartner, and P. Stabeno, 2011: On ocean and sea ice modes of variability in the Bering Sea. *Journal of Geophysical Research: Oceans*, **116 (C12)**, n/a–n/a, doi:10.1029/2011JC007389, URL http://dx.doi.org/10.1029/2011JC007389, c12034.

Dietrich, J., and Coauthors, 2011: Modeling hurricane waves and storm surge using integrally-coupled, scalable computations. *Coastal Engineering*, **58 (1)**, 45–65, doi:10.1016/j.coastaleng.2010.08.001.

Dietrich, J. C., and Coauthors, 2010: A high-resolution coupled riverine flow, tide, wind, wind wave, and storm surge model for southern louisiana and mississippi. part ii: Synoptic description and analysis of hurricanes katrina and rita. *Monthly Weather Review*, **138 (2)**, 378–404, doi: 10.1175/2009MWR2907.1.

Dietrich, J. C., and Coauthors, 2012: Performance of the unstructured-mesh, swan+adcirc model in computing hurricane waves and surge. *Journal of Scientific Computing*, **52 (2)**, 468–497, doi:10.1007/s10915-011-9555-6, URL http://dx.doi.org/10.1007/s10915-011-9555-6.

Egbert, G. D., A. F. Bennett, and M. G. G. Foreman, 1994: TOPEX/POSEIDON tides estimated using a global inverse model. *Journal of Geophysical Research: Oceans*, **99 (C12)**, 24 821–24 852, doi:10.1029/94JC01894, URL http://dx.doi.org/10.1029/94JC01894.

Egbert, G. D., and S. Y. Erofeeva, 2002: Efficient Inverse Modeling of Barotropic Ocean Tides. *Journal of Atmospheric and Oceanic Technology*, **19 (2)**, 183–204, doi:10.1175/1520-0426(2002)019⟨0183:EIMOBO⟩2.0.CO;2.

Erikson, L. H., R. T. Mccall, A. V. Rooijen, and B. Norris, 2015: Hindcast storm events in the Bering Sea for the St. Lawrence Island and Unalakleet Regions, Alaska. Open-File Report.

Foreman, M. G. G., P. F. Cummins, J. Y. Cherniawsky, and P. Stabeno, 2006: Tidal energy in the Bering Sea. *Journal of Marine Research*, **64 (6)**, doi:doi:10.1357/002224006779698341.

Fujisaki, A., H. Yamaguchi, T. Toyota, A. Futatsudera, and M. Miyanaga, 2009: Measurements of air-ice drag coefficient over the ice-covered Sea of Okhotsk. *Journal of Oceanography*, **65 (4)**, 487–498, doi:10.1007/s10872-009-0042-8.

Garbrecht, T., C. Lüpkes, J. Hartmann, and M. Wolff, 2002: Atmospheric drag coefficients over sea icevalidation of a parameterization concept. *Tellus A*, **54**, 205–219.

Garratt, J. R., 1977: Review of Drag Coefficients over Oceans and Continents. *Monthly Weather Review*, **105 (7)**, 915–929, doi:10.1175/1520-0493(1977)105⟨0915:RODCOO⟩2.0.CO;2.

GEBCO, 2014: The GEBCO 2014 Grid, version 20141201. www.gebco.net.

Grumbine, R. W., 1996: Automated Passive Microwave Sea Ice Concentration Analysis at NCEP. Technical Note 120.

Grumbine, R. W., 2014: Automated Sea Ice Concentration Analysis History at NCEP 1996-2012. MMAB Technical Note 321.

Homer, C., and Coauthors, 2015: Completion of the 2011 National Land Cover Database for the conterminous United States-Representing a decade of land cover change information. *Photogrammetric Engineering and Remote Sensing*, **81 (5)**, 345–354.

Jakobsson, M., and Coauthors, 2012: The International Bathymetric Chart of the Arctic Ocean (IBCAO) Version 3.0. Geophysical Research Letters.

Johnson, W. R., and Z. Kowalik, 1986: Modeling of storm surges in the Bering Sea and Norton Sound. *Journal of Geophysical Research: Oceans*, **91 (C4)**, 5119–5128, doi:10.1029/JC091iC04p05119.

Kinsman, N. E., and M. Deraps, 2012: Coastal hazard field investigations in response to the November 2011 Bering Sea storm, Norton Sound, Alaska. Alaska DNR, Division of Geological and Geophysical Surveys Report.

Kowalik, Z., 1984: Storm surges in the Beaufort and Chukchi Seas. *Journal of Geophysical Research: Oceans*, **89 (C6)**, 10 570–10 578, doi:10.1029/JC089iC06p10570.

Kowalik, Z., 1999: Bering Sea Tides. *Dynamics of the Bering Sea: A Summary of Physical, Chemical, and Biological Characteristics, and a Synopsis of Research on the Bering Sea (Alaska Sea*

Grant College Program Report, No. 99-03.), T. R. Loughlin, Ed., Univ of Alaska Sea Grant, chap. 4, 93–127.

Lim, E., B. Eakins, and R. Caldwell, 2011a: Digital Elevation Models of Akutan, Alaska: Procedures, Data Sources and Analysis. U.S. Dept. of Commerce, Boulder, CO, 29 pp., NOAA Technical Memorandum NESDIS NGDC-42.

Lim, E., B. Eakins, and R. Wigley, 2011b: Coastal Relief Model of Southern Alaska: Procedures, Data Sources and Analysis. 22 pp., NOAA Technical Memorandum NESDIS NGDC-43.

Lu, P., Z. Li, B. Cheng, and M. Leppranta, 2011: A parameterization of the ice-ocean drag coefficient. *Journal of Geophysical Research: Oceans*, **116 (C7)**, n/a–n/a, doi:10.1029/2010JC006878, c07019.

Lüpkes, C., and G. Birnbaum, 2005: Surface Drag in the Arctic Marginal Sea-ice Zone: A Comparison of Different Parameterisation Concepts. *Boundary-Layer Meteorology*, **117 (2)**, 179–211, doi:10.1007/s10546-005-1445-8.

Lüpkes, C., V. M. Gryanik, J. Hartmann, and E. L. Andreas, 2012: A parametrization, based on sea ice morphology, of the neutral atmospheric drag coefficients for weather prediction and climate models. *Journal of Geophysical Research: Atmospheres*, **117 (D13)**, n/a–n/a, doi:10.1029/2012JD017630, URL http://dx.doi.org/10.1029/2012JD017630, d13112.

Lüpkes, C., V. M. Gryanik, A. Rsel, G. Birnbaum, and L. Kaleschke, 2013: Effect of sea ice morphology during Arctic summer on atmospheric drag coefficients used in climate models. *Geophysical Research Letters*, **40 (2)**, 446–451, doi:10.1002/grl.50081.

Macklin, S. A., 1983: Wind drag coefficient over first-year sea ice in the Bering Sea. *Journal of Geophysical Research: Oceans*, **88 (C5)**, 2845–2852, doi:10.1029/JC088iC05p02845, URL http://dx.doi.org/10.1029/JC088iC05p02845.

Medley, P., L. Taylor, B. Eakins, K. Carignan, R. Warnken, and E. Lim, 2009: Digital Elevation Models of Chignik, Alaska: Procedures, Data Sources and Analysis. U.S. Dept. of Commerce, Boulder, CO, 26 pp., NOAA Technical Memorandum NESDIS NGDC-28.

Mesquita, M. S., D. E. Atkinson, and K. I. Hodges, 2010: Characteristics and Variability of Storm Tracks in the North Pacific, Bering Sea, and Alaska. *Journal of Climate*, **23 (2)**, 294–311, doi: 10.1175/2009JCLI3019.1.

NOAA, ????: Tides & currents products. Accessed: 2013-09-30, https://tidesandcurrents.noaa.gov/products.html.

Pawlowicz, R., B. Beardsley, and S. Lentz, 2002: Classical tidal harmonic analysis including error estimates in matlab using t tide. *Comput. Geosci.*, **28 (8)**, 929–937, doi:10.1016/S0098-3004(02)00013-4, URL http://dx.doi.org/10.1016/S0098-3004(02)00013-4.

Rienecker, M. M., and M. D. Teubner, 1980: Joumal of marine research, 42, 473-485. rienecker, m.m. and m.d. teubner, 1980. a note on frictional effects in taylor's problem. *Joumal of Marine Research*, **42**, 473485.

Saha, S., and Coauthors, 2014: The NCEP Climate Forecast System Version 2. *Journal of Climate*, **27 (6)**, 2185–2208, doi:10.1175/JCLI-D-12-00823.1.

Smithson, M., 1992: Pelagic tidal constants - 3. iapso publication scientifique no.35. International Association for the Physical Sciences of the Ocean (IAPSO) of the International Union of Geodesy and Geophysics.

Spreen, G., R. Kwok, and D. Menemenlis, 2011: Trends in arctic sea ice drift and role of wind forcing: 19922009. *Geophysical Research Letters*, **38 (19)**, doi:10.1029/2011GL048970, URL http://dx.doi.org/10.1029/2011GL048970, l19501.

Taylor, L., B. Eakins, K. Carignan, R. Warnken, D. Schoolcraft, T. Sazonova, , and G. Sharman, 2008: Digital Elevation Model of Dutch Harbor, Alaska: Procedures, Data Sources and Analysis. U.S. Dept. of Commerce, Boulder, CO, 25 pp., NOAA Technical Memorandum NESDIS NGDC-4.

Tsamados, M., D. L. Feltham, D. Schroeder, D. Flocco, S. L. Farrell, N. Kurtz, S. W. Laxon, and S. Bacon, 2014: Impact of Variable Atmospheric and Oceanic Form Drag on Simulations of Arctic Sea Ice. *Journal of Physical Oceanography*, **44 (5)**, 1329–1353, doi:10.1175/JPO-D-13-0215.1.

Westerink, J. J., R. A. Luettich, and J. C. Muccino, 1994: Modelling tides in the western North Atlantic using unstructured graded grids. *Tellus A*, **46 (2)**, 178–199, doi:10.1034/j.1600-0870.1994.00007.x, URL http://dx.doi.org/10.1034/j.1600-0870.1994.00007.x.

Westerink, J. J., and Coauthors, 2008: A basin- to channel-scale unstructured grid hurricane storm surge model applied to southern louisiana. *Monthly Weather Review*, **136 (3)**, 833–864, doi:10.1175/2007MWR1946.1.

Zaron, E. D., and G. D. Egbert, 2006: Estimating open-ocean barotropic tidal dissipation: The hawaiian ridge. *Journal of Physical Oceanography*, **36 (6)**, 1019–1035, doi:10.1175/JPO2878.1.

Zippel, S., and J. Thompson, 2016: Air-sea interactions in the marginal ice zone. *Elem Sci Anth*, **4 (95)**, doi:doi:10.12952/journal.elementa.000095.

LIST OF TABLES

Table 1. Measured and analyzed difference statistics (R^2, standard deviation, average error, absolute average error and normalized root mean square error) for the 4 main tidal constituents at all 121 stations. Also included are the absolute difference statistics considering all 8 astronomical constituents. Amplitude error and standard deviation is in meters while phase error and standard deviation is in degrees 33

Table 2. Root mean square error (unitless) and average peak error (in meters) at each available station for all storms simulations. For storms which occurred in the presence of ice, error metrics are shown for runs with and without considering ice coverage. 34

Table 3. Major peak and trough water surface elevation values for the simulated storms in periods of ice coverage. Peak values (in meters) and timings are shown for observed peaks, model runs without ice coverage, and model runs considering ice coverage. Peak errors (in meters) are also shown comparing model data to observed data. 35

TABLE 1. Measured and analyzed difference statistics (R^2, standard deviation, average error, absolute average error and normalized root mean square error) for the 4 main tidal constituents at all 121 stations. Also included are the absolute difference statistics considering all 8 astronomical constituents. Amplitude error and standard deviation is in meters while phase error and standard deviation is in degrees

Constituent	R^2	Std-Dev	Avg-Err	Abs-Avg-Err	Norm-RMSE
O_1 Amplitude	0.845	0.048	-0.013	0.024	0.173
K_1 Amplitude	0.899	0.061	-0.004	0.034	0.137
N_2 Amplitude	0.947	0.036	-0.004	0.019	0.137
M_2 Amplitude	0.962	0.157	-0.015	0.080	0.125
O_1 Phase	0.902	27.748	-5.908	12.374	0.112
K_1 Phase	0.921	33.776	9.759	16.099	0.136
N_2 Phase	0.953	22.874	3.609	10.957	0.097
M_2 Phase	0.956	23.904	2.422	11.309	0.096
All Amplitude	0.976	0.065	-0.006	0.026	0.127
All Phase	0.907	33.707	0.658	16.571	0.132

TABLE 2. Root mean square error (unitless) and average peak error (in meters) at each available station for all storms simulations. For storms which occurred in the presence of ice, error metrics are shown for runs with and without considering ice coverage.

August 2012	Nome	RDD	Prudhoe Bay	Unalakleet
RMSE (no ice)	0.154	0.141	0.091	–
Avg. PE (no ice)	0.052	0.058	0.067	–
November 2011	Nome	RDD	Prudhoe Bay	Unalakleet
RMSE (no ice)	0.198	0.148	0.156	–
RMSE (ice)	0.200	0.175	0.167	–
Avg. PE (no ice)	-0.698	-0.282	-0.279	–
Avg. PE (ice)	-0.385	-0.365	-0.164	–
February 2011	Nome	RDD	Prudhoe Bay	Unalakleet
RMSE (no ice)	0.171	0.152	0.161	–
RMSE (ice)	0.143	0.138	0.164	–
Avg. PE (no ice)	-0.248	-0.293	-0.251	–
Avg. PE (ice)	-0.159	-0.211	-0.245	–
January 2017	Nome	RDD	Prudhoe Bay	Unalakleet
RMSE (no ice)	0.146	0.167	0.166	0.282
RMSE (ice)	0.232	0.232	0.163	0.346
Avg. PE (no ice)	-0.226	-0.098	0.105	-0.407
Avg. PE (ice)	0.055	0.176	0.205	0.050

TABLE 3. Major peak and trough water surface elevation values for the simulated storms in periods of ice coverage. Peak values (in meters) and timings are shown for observed peaks, model runs without ice coverage, and model runs considering ice coverage. Peak errors (in meters) are also shown comparing model data to observed data.

November 2011	**Nome**				**Red Dog Dock**					**Prudhoe Bay**			**Unalakleet**		
Peak	1	2	3		1	2	3 (trough)			1					
Time (obsv)	11/9 10:12	11/9 15:00	11/10 2:00	–	11/10 9:48	11/11 12:41	11/13 6:00	–	–	11/11 10:47	–	–	–	–	–
Time (model, no ice)	11/9 10:53	11/9 16:18	11/10 6:48	–	11/10 11:48	11/11 10:35	11/13 7:18	–	–	11/11 9:53	–	–	–	–	–
Time (model, ice)	11/9 10:47	11/9 16:18	11/10 7:00	–	11/10 11:48	11/11 10:35	11/13 9:17	–	–	11/11 9:53	–	–	–	–	–
Peak (obsv)	1.952	1.769	2.778	–	1.665	0.693	-0.842	–	–	0.426	–	–	–	–	–
Peak (model, no ice)	1.522	1.296	1.587	–	0.9778	0.5077	-0.8145	–	–	0.1475	–	–	–	–	–
Peak (model, ice)	1.934	1.516	1.893	–	1.13	0.6199	-1.33	–	–	-0.0167	–	–	–	–	–
Peak error (no ice)	-0.43	-0.473	-1.191	–	-0.6872	-0.1853	0.0275	–	–	-0.2785	–	–	–	–	–
Peak error (ice)	-0.018	-0.253	-0.885	–	-0.535	-0.0731	-0.488	–	–	-0.1642	–	–	–	–	–
February 2011	**Nome**				**Red Dog Dock**					**Prudhoe Bay**			**Unalakleet**		
Peak	1	2	3		1	2	3			1	2	3			
Time (obsv)	2/18 1:06	2/21 3:29	2/24 20:24	–	2/18 10:00	2/21 12:47	2/25 7:53	–	–	2/19 10:35	2/24 13:18	2/26 5:30	–	–	–
Time (model, no ice)	2/18 1:41	2/21 4:18	2/24 18:42	–	2/18 11:00	2/21 12:23	2/25 8:48	–	–	2/19 11:00	2/24 15:35	2/26 5:54	–	–	–
Time (model, ice)	2/18 1:41	2/21 4:18	2/24 18:42	–	2/18 11:00	2/21 12:23	2/25 7:53	–	–	2/19 11:00	2/24 15:35	2/26 5:54	–	–	–
Peak (obsv)	1.14	1.005	1.903	–	1.431	0.76	2.131	–	–	0.618	0.678	1.045	–	–	–
Peak (model, no ice)	0.7443	0.9454	1.615	–	0.994	0.7431	1.707	–	–	0.3381	0.5	0.7513	–	–	–
Peak (model, ice)	0.8521	0.9875	1.731	–	1.096	0.78	1.814	–	–	0.3426	0.4735	0.7914	–	–	–
Peak error (no ice)	-0.3957	-0.0596	-0.288	–	-0.437	-0.0169	-0.424	–	–	-0.2799	-0.178	-0.2937	–	–	–
Peak error (ice)	-0.2879	-0.0175	-0.172	–	-0.335	0.02	-0.317	–	–	-0.2754	-0.2045	-0.2536	–	–	–
January 2017	**Nome**				**Red Dog Dock**					**Prudhoe Bay**			**Unalakleet**		
Peak	1	2	3	4 (trough)	1	2	3	4	5 (trough)	1	2	3 (trough)	1	2	3
Time (obsv)	12/30 15:05	12/31 1:53	1/1 14:42	12/26 5:36	12/30 17:11	12/31 2:54	1/1 9:48	1/5 6:48	12/26 15:29	1/5 21:11	1/7 20:05	1/7 1:12	12/30 8:36	12/31 8:24	1/1 12:00
Time (model, no ice)	12/30 14:42	12/31 2:11	1/1 15:29	12/26 6:48	12/30 19:12	12/31 4:35	1/1 11:05	1/5 8:30	12/26 15:41	1/5 21:54	1/8 3:41	1/7 3:00	12/30 10:59	12/31 9:29	1/1 11:54
Time (model, ice)	12/30 15:54	12/31 2:05	1/1 14:54	12/26 6:48	12/30 19:12	12/31 4:35	1/1 11:05	1/5 8:30	12/26 16:59	1/5 22:00	1/8 3:41	1/7 3:00	12/30 11:54	12/31 9:23	1/1 11:54
Peak (obsv)	1.621	1.696	2.142	-0.117	1.259	1.955	1.317	1.118	-0.344	0.951	0.551	-0.268	2.163	2.527	2.321
Peak (model, no ice)	1.287	1.467	1.834	-0.15	1.283	1.397	1.301	1.141	-0.3057	0.9329	0.6702	-0.0529	1.688	2.183	1.92
Peak (model, ice)	1.662	2.191	2.187	-0.476	1.727	1.887	1.579	1.634	-0.641	1.23	0.7937	-0.176	2.043	3.032	2.086
Peak error (no ice)	-0.334	-0.229	-0.308	-0.033	0.024	-0.558	-0.016	0.023	0.0383	-0.0181	0.1192	0.2151	-0.475	-0.344	-0.401
Peak error (ice)	0.041	0.495	0.045	-0.359	0.468	-0.068	0.262	0.516	-0.297	0.279	0.2427	0.092	-0.12	0.505	-0.235

LIST OF FIGURES

Fig. 1. Study region (source: Google Earth) and NOAA and IAPSO station locations used for tidal validation. Stations used to validate storm surge water surface elevations are shown in red and labeled. 38

Fig. 2. ADCIRC Alaska model domain and bathymetry/topography in meters. 39

Fig. 3. Detail of the Yukon-Kuskokwim delta bathymetry/topography (meters) as represented in the Alaska ADCIRC model. 40

Fig. 4. Yukon-Kuskokwim delta Manning's n values as represented in the ADCIRC Alaska model. . . . 41

Fig. 5. Drag coefficient, C_d, parameterization used in the presence of ice as a function of area fraction ice coverage and 10 meter wind speed. 42

Fig. 6. Percent change in C_d when comparing the parameterization of air-sea drag to the standard Garratt drag law (under no ice conditions). The black lines represent no change in drag coefficient when ice is considered. 43

Fig. 7. Maximum water surface elevation for the 90 day tide only simulation. 44

Fig. 8. Amplitudes (left, in meters) and phases (right, in degrees) for the K_1, O_1, M_2 and N_2 tidal constituents as computed by ADCIRC. 45

Fig. 9. Detail of the amplitudes (left, in meters) and phases (right, in degrees) for the K_1, O_1, M_2 and N_2 tidal constituents in the Bering and Chukchi Seas as computed by ADCIRC. 46

Fig. 10. ADCIRC modeled versus observed comparison of amplitudes (in meters) and phases (in degrees) for the K_1, O_1, M_2 and N_2 tidal constituents. The lines show a difference of Δ from the observed values. The best fit line with slope is shown. 47

Fig. 11. Validation of amplitudes (in meters) and phases (in degrees) at each tidal station for the K_1, O_1, M_2 and N_2 tidal constituents. Error bins are +/- 40% or 4 cm, +/- 30% or 3 cm, +/- 20% or 2 cm and +/- 10% or 1 cm for the amplitudes and +/- 40°, +/- 30°, +/- 20° and +/- 10° for the phases. 48

Fig. 12. Maximum tidal currents (in ms^{-1}), with detail along the Aleutian Islands 49

Fig. 13. Windspeed (left) and water surface elevation (without tides) for the August 2012 storm as computed by ADCIRC. Fields shown are for August 15 0:00 UTC, August 15 20:00 UTC, August 16 16:00 UTC, August 17 12:00 UTC and August 18 8:00 UTC. 50

Fig. 14. Validation of CFSv2 pressure, windspeed and direction for August 2012 for Nome (9468756), Red Dog Dock (9491094) and Prudhoe Bay (9497645). 51

Fig. 15. Validation of water surface elevation as computed by ADCIRC for August 2012 for Nome (9468756), Red Dog Dock (9491094) and Prudhoe Bay (9497645). 52

Fig. 16. Ice coverage (in terms of area fraction, AF) during November 2011 storm (November 7th, 2011 6:00 UTC), February 2011 storm (February 23rd, 2011 3:00 UTC), and January 2017 storm (January 1, 2017 0:00 UTC). 53

Fig. 17. Windspeed (left) and water surface elevation without tides (right) for the November 2011 storm. Fields shown are for November 8 10:00 UTC, November 9 6:00 UTC, November 10 2:00 UTC, November 10 22:00 UTC and November 11 18:00 UTC. 54

Fig. 18. Validation of CFSv2 pressure, windspeed and direction for November 2011 for Nome (9468756), Red Dog Dock (9491094) and Prudhoe Bay (9497645). 55

Fig. 19. Validation of water surface elevation as computed by ADCIRC for November 2011 for Nome (9468756), Red Dog Dock (9491094) and Prudhoe Bay (9497645) with (gold) and without ice (red). 56

Fig. 20. Effect of sea ice on maximum modeled water surface elevation for November 2011, February 2011 and January 2017 57

Fig. 21. Windspeed (left) and water surface elevation without tides (right) for the February 2011 storm. Fields shown are for February 22 12:00 UTC, February 23 8:00 UTC, February 24 4:00 UTC, February 25 0:00 UTC, and February 25 20:00 UTC. 58

Fig. 22. Validation of CFSv2 pressure, windspeed and direction for February 2011 for Nome (9468756), Red Dog Dock (9491094) and Prudhoe Bay (9497645). 59

Fig. 23. Validation of water surface elevation as computed by ADCIRC for February 2011 for Nome (9468756), Red Dog Dock (9491094) and Prudhoe Bay (9497645), with (gold) and without ice (red). 60

Fig. 24. Windspeed (left) and water surface elevation without tides (right) for the January 2017 storm. Fields shown are for December 29 2:00 UTC, December 30 3:00 UTC, December 31 4:00 UTC, January 1 5:00 UTC, and Janury 2 6:00 UTC. 61

Fig. 25. Validation of CFSv2 pressure, windspeed and direction for February 2011 for Nome (9468756), Unalakleet (9468333) and Red Dog Dock (9491094). The Prudhoe Bay (9497645) meterological station was inactive during this event. 62

Fig. 26. Validation of water surface elevation as computed by ADCIRC for January 2017 for Nome (9468756), Unalakleet (9468333), Red Dog Dock (9491094) and Prudhoe Bay (9497645), with (gold) and without ice (red). 63

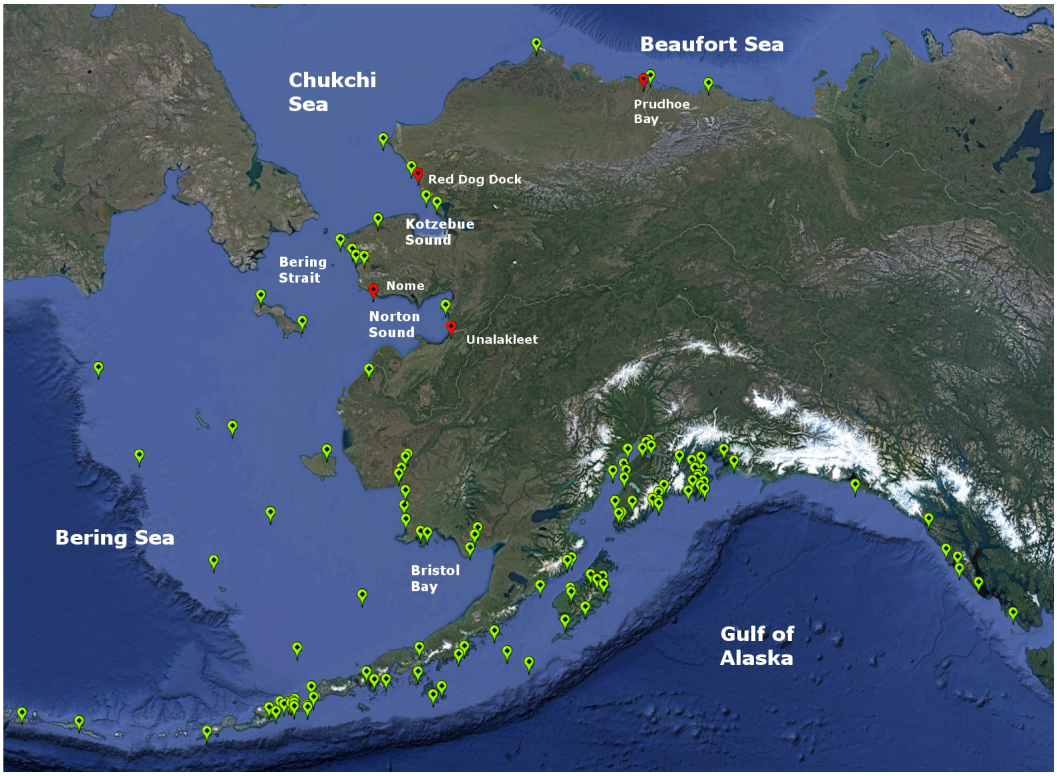

FIG. 1. Study region (source: Google Earth) and NOAA and IAPSO station locations used for tidal validation. Stations used to validate storm surge water surface elevations are shown in red and labeled.

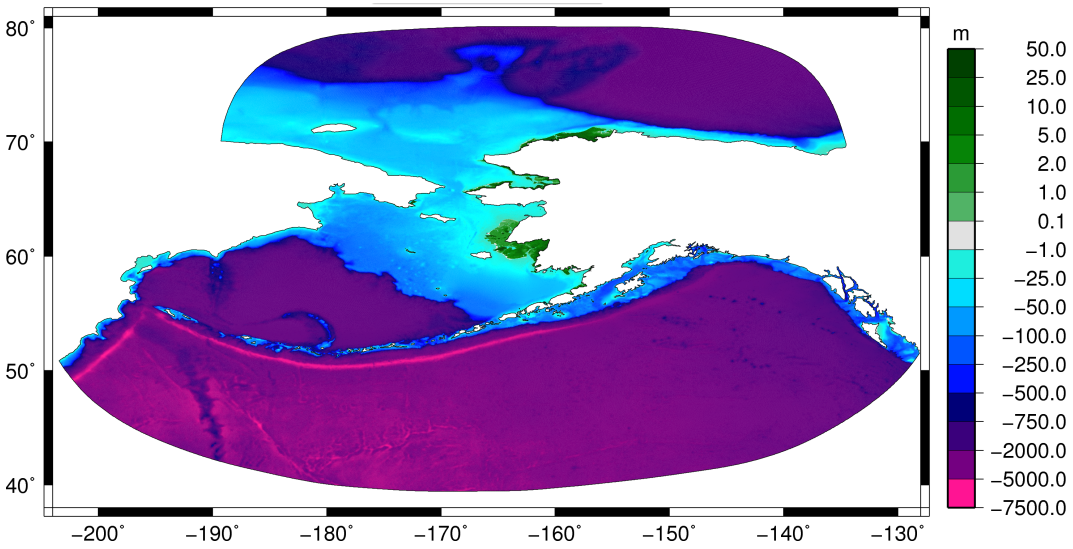

FIG. 2. ADCIRC Alaska model domain and bathymetry/topography in meters.

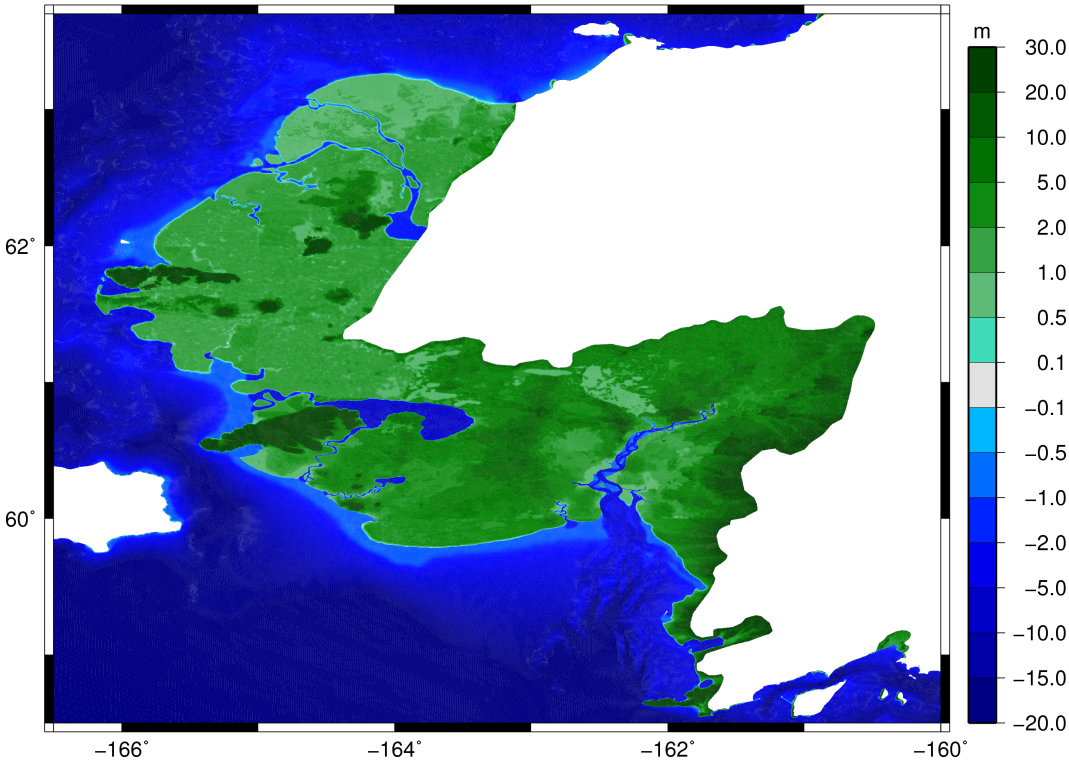

FIG. 3. Detail of the Yukon-Kuskokwim delta bathymetry/topography (meters) as represented in the Alaska ADCIRC model.

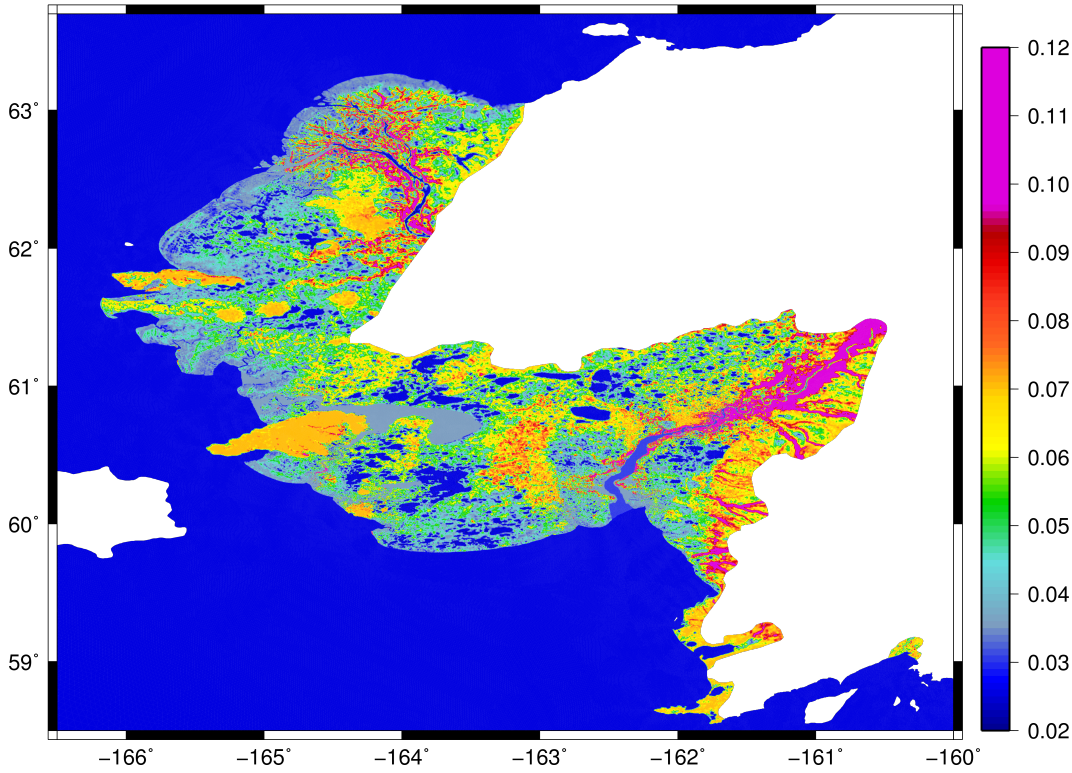

FIG. 4. Yukon-Kuskokwim delta Manning's *n* values as represented in the ADCIRC Alaska model.

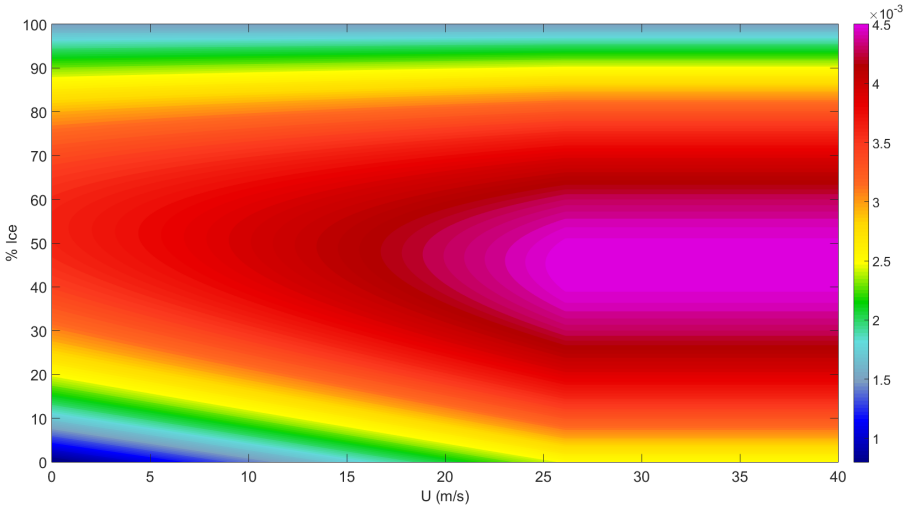

FIG. 5. Drag coefficient, C_d, parameterization used in the presence of ice as a function of area fraction ice coverage and 10 meter wind speed.

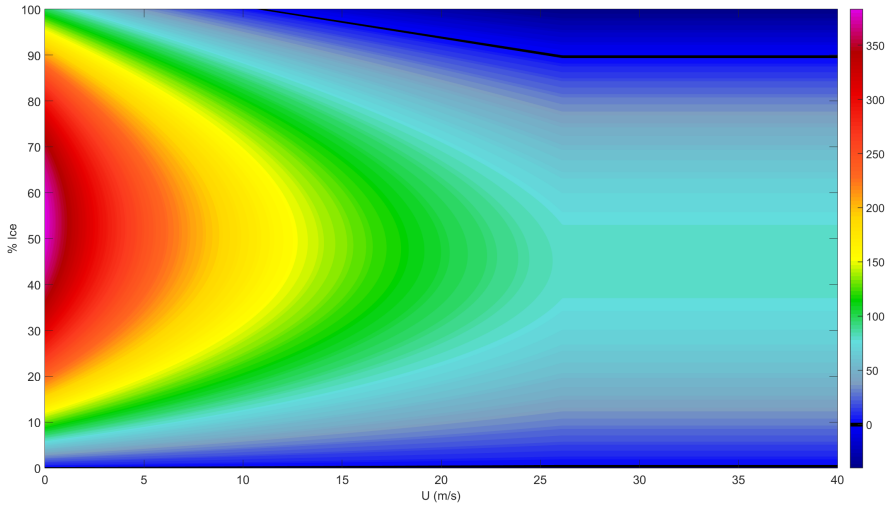

FIG. 6. Percent change in C_d when comparing the parameterization of air-sea drag to the standard Garratt drag law (under no ice conditions). The black lines represent no change in drag coefficient when ice is considered.

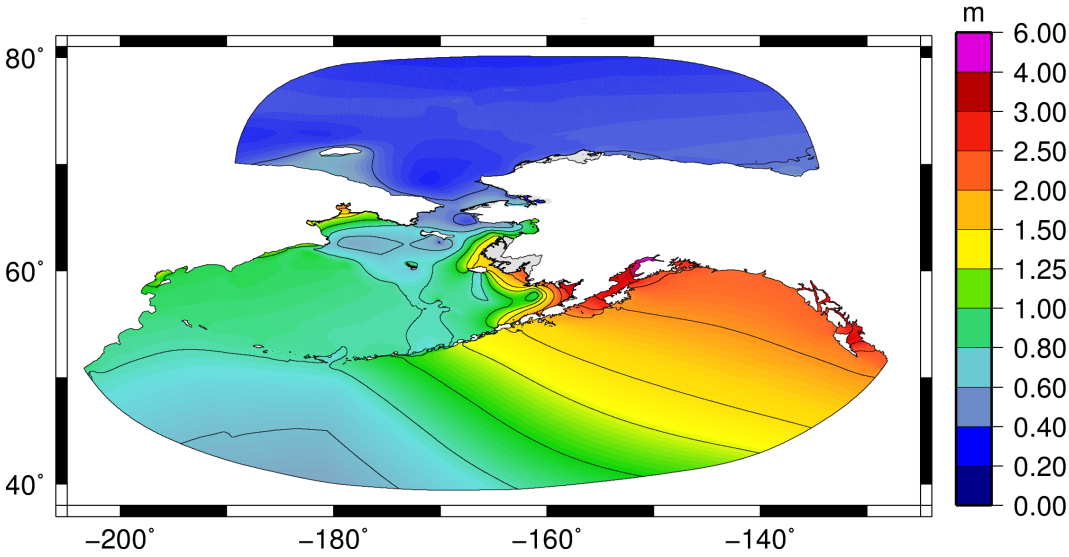

FIG. 7. Maximum water surface elevation for the 90 day tide only simulation.

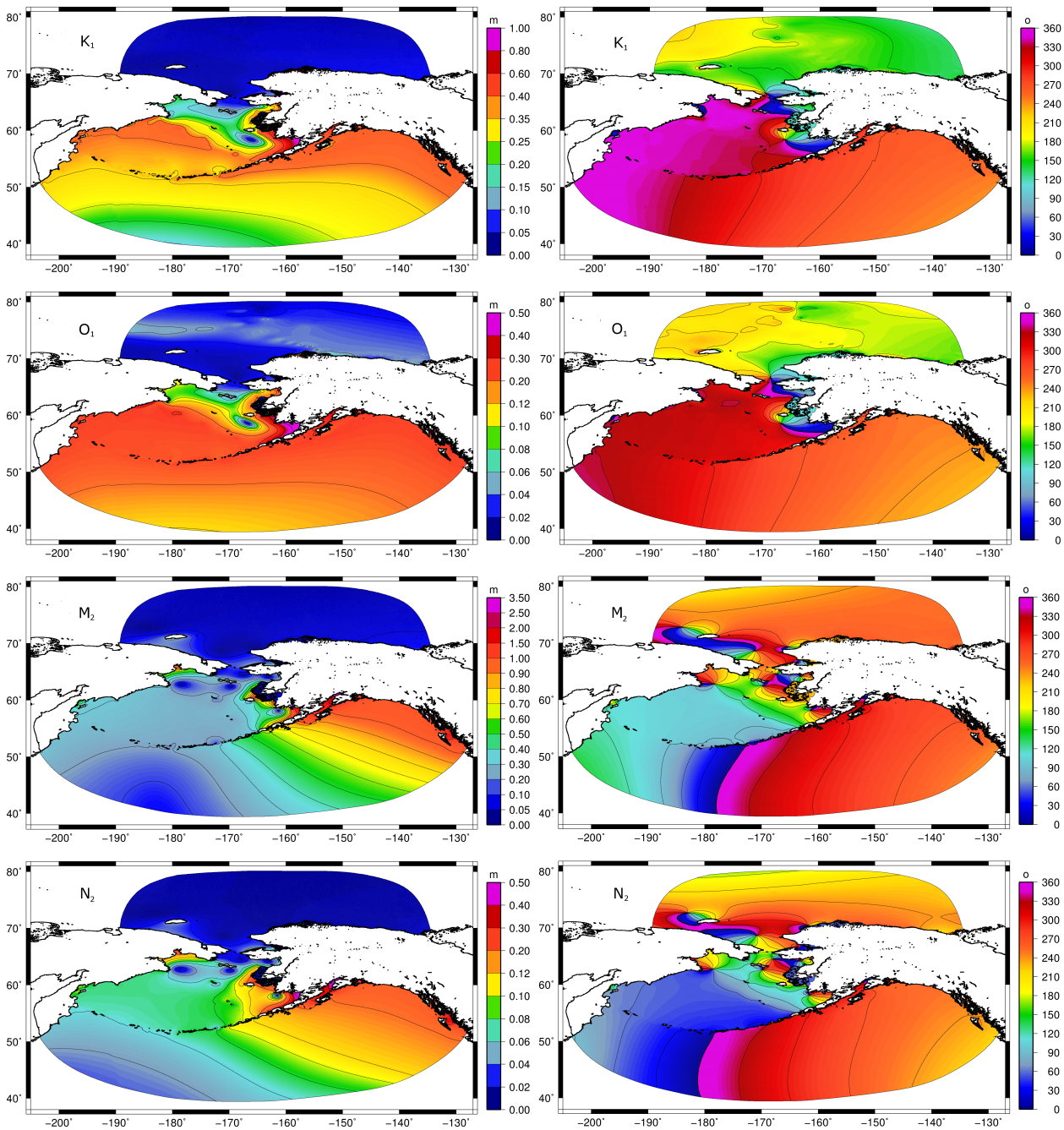

FIG. 8. Amplitudes (left, in meters) and phases (right, in degrees) for the K_1, O_1, M_2 and N_2 tidal constituents as computed by ADCIRC.

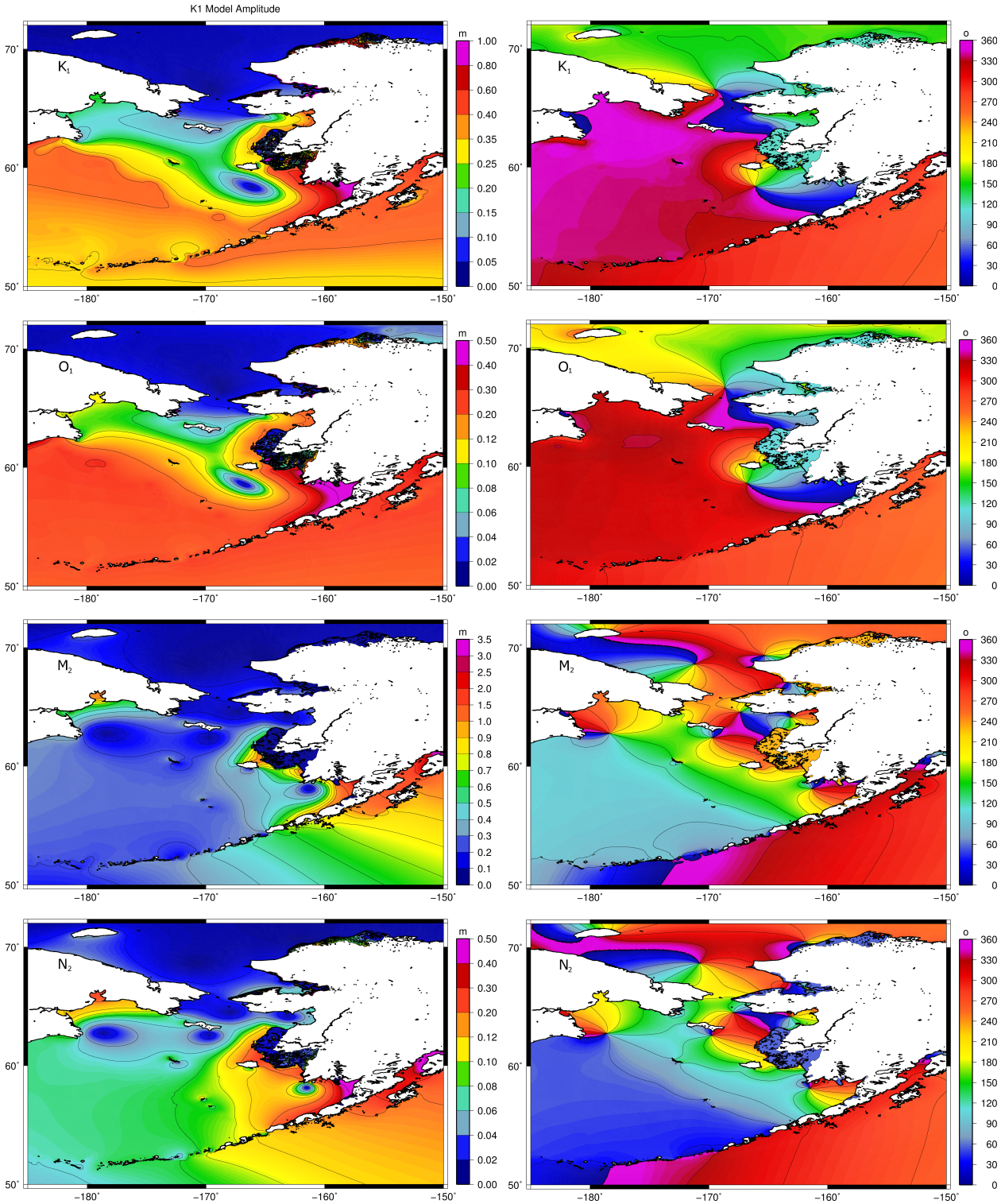

FIG. 9. Detail of the amplitudes (left, in meters) and phases (right, in degrees) for the K_1, O_1, M_2 and N_2 tidal constituents in the Bering and Chukchi Seas as computed by ADCIRC.

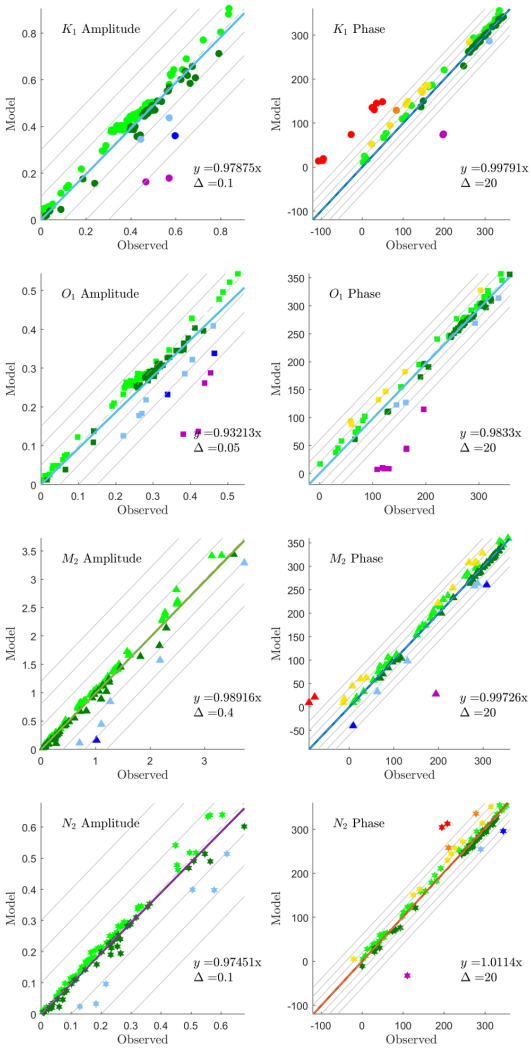

FIG. 10. ADCIRC modeled versus observed comparison of amplitudes (in meters) and phases (in degrees) for the K_1, O_1, M_2 and N_2 tidal constituents. The lines show a difference of Δ from the observed values. The best fit line with slope is shown.

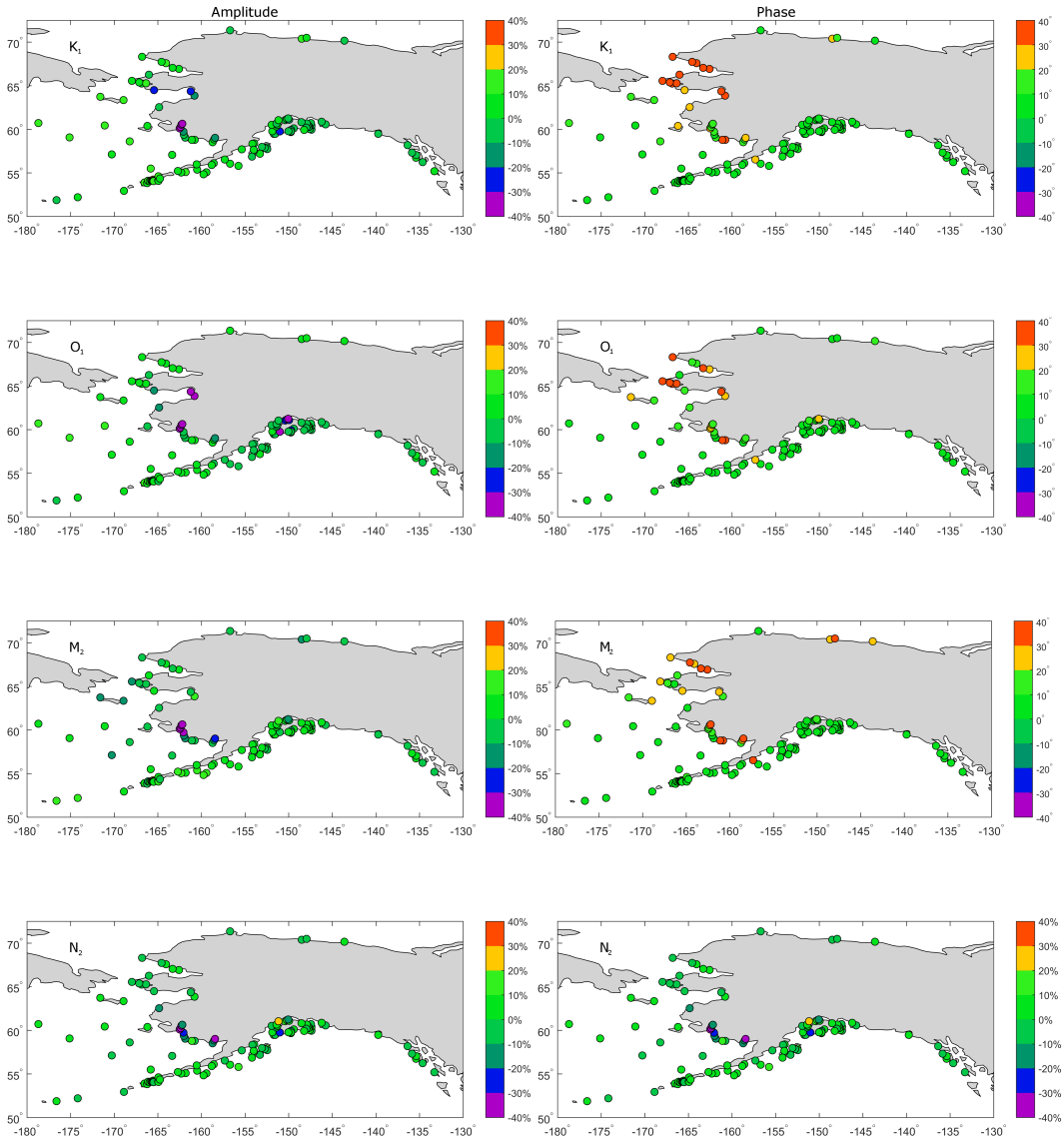

FIG. 11. Validation of amplitudes (in meters) and phases (in degrees) at each tidal station for the K_1, O_1, M_2 and N_2 tidal constituents. Error bins are +/- 40% or 4 cm, +/- 30% or 3 cm, +/- 20% or 2 cm and +/- 10% or 1 cm for the amplitudes and +/- 40°, +/- 30°, +/- 20° and +/- 10° for the phases.

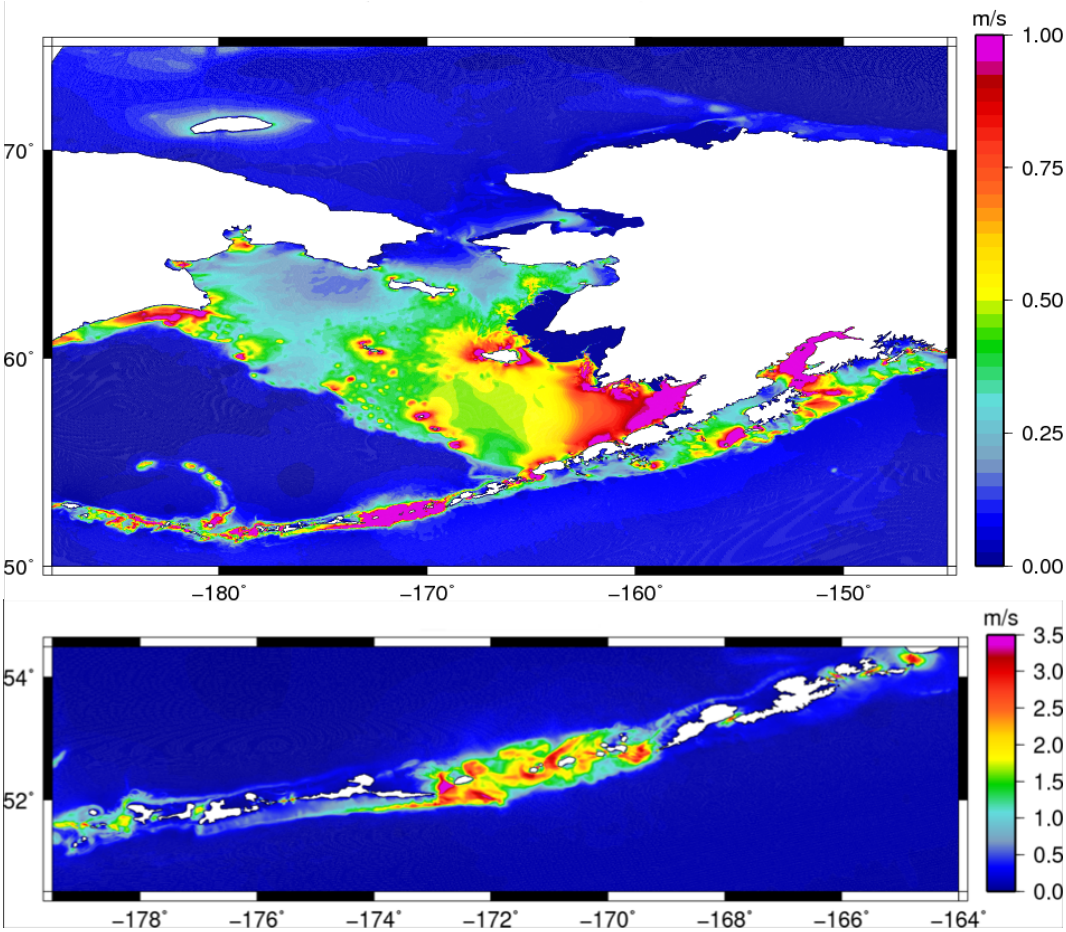

FIG. 12. Maximum tidal currents (in ms^{-1}), with detail along the Aleutian Islands

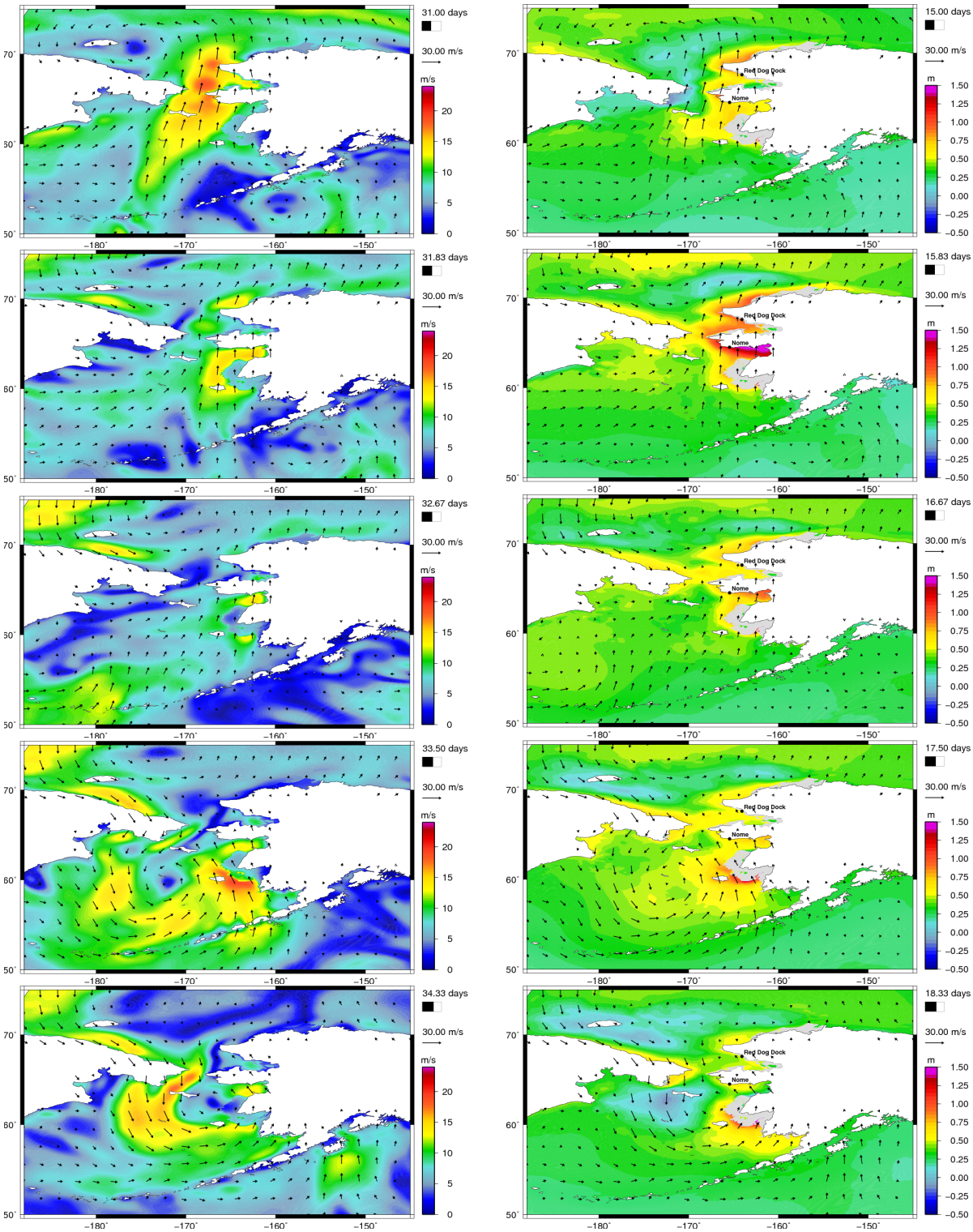

FIG. 13. Windspeed (left) and water surface elevation (without tides) for the August 2012 storm as computed by ADCIRC. Fields shown are for August 15 0:00 UTC, August 15 20:00 UTC, August 16 16:00 UTC, August 17 12:00 UTC and August 18 8:00 UTC.

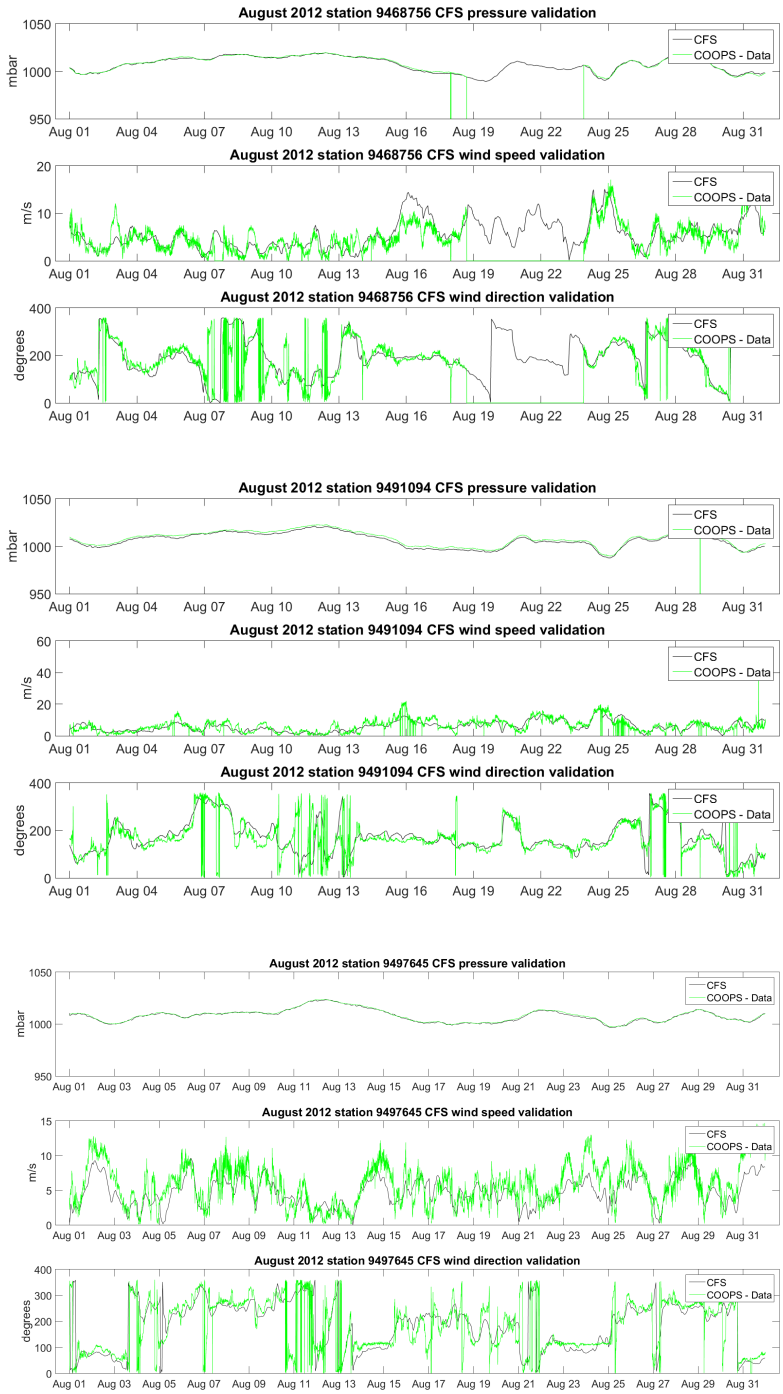

FIG. 14. Validation of CFSv2 pressure, windspeed and direction for August 2012 for Nome (9468756), Red Dog Dock (9491094) and Prudhoe Bay (9497645).

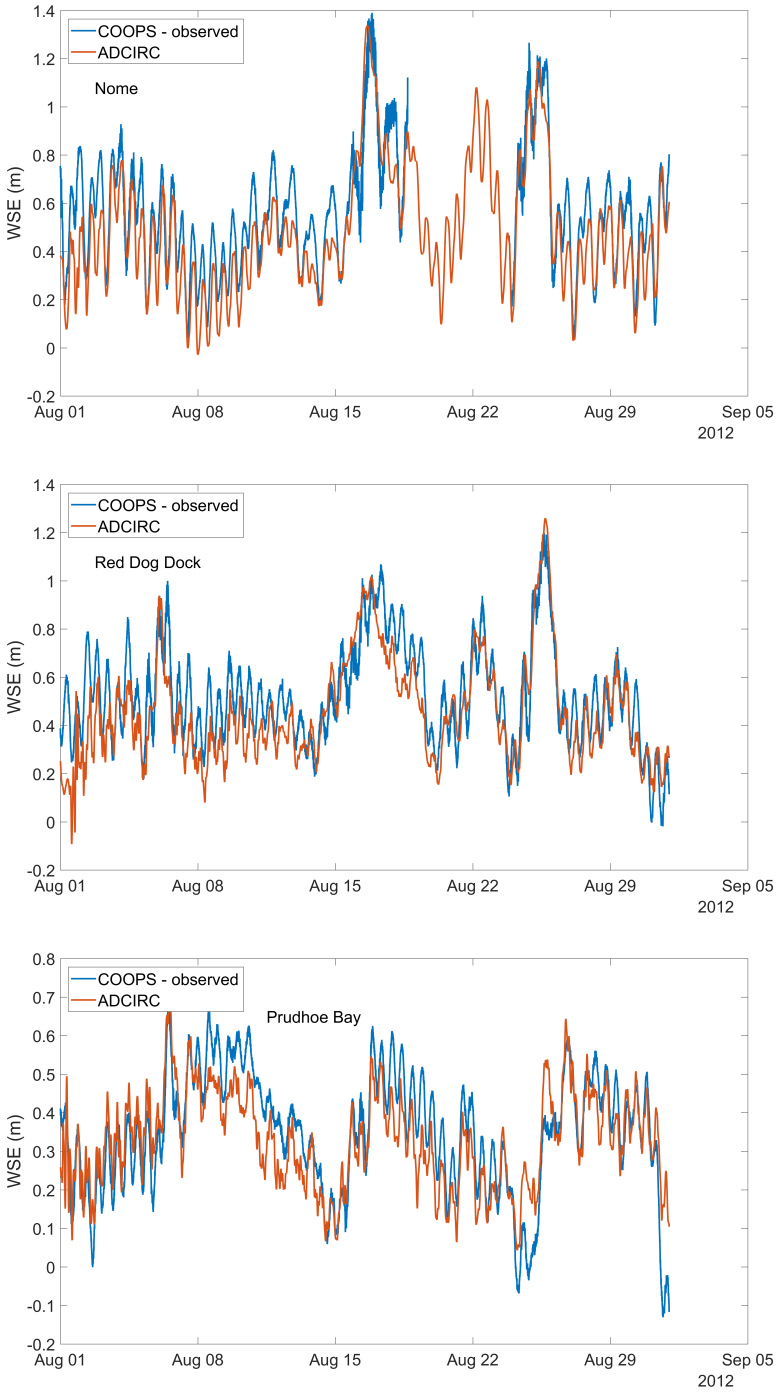

FIG. 15. Validation of water surface elevation as computed by ADCIRC for August 2012 for Nome (9468756), Red Dog Dock (9491094) and Prudhoe Bay (9497645).

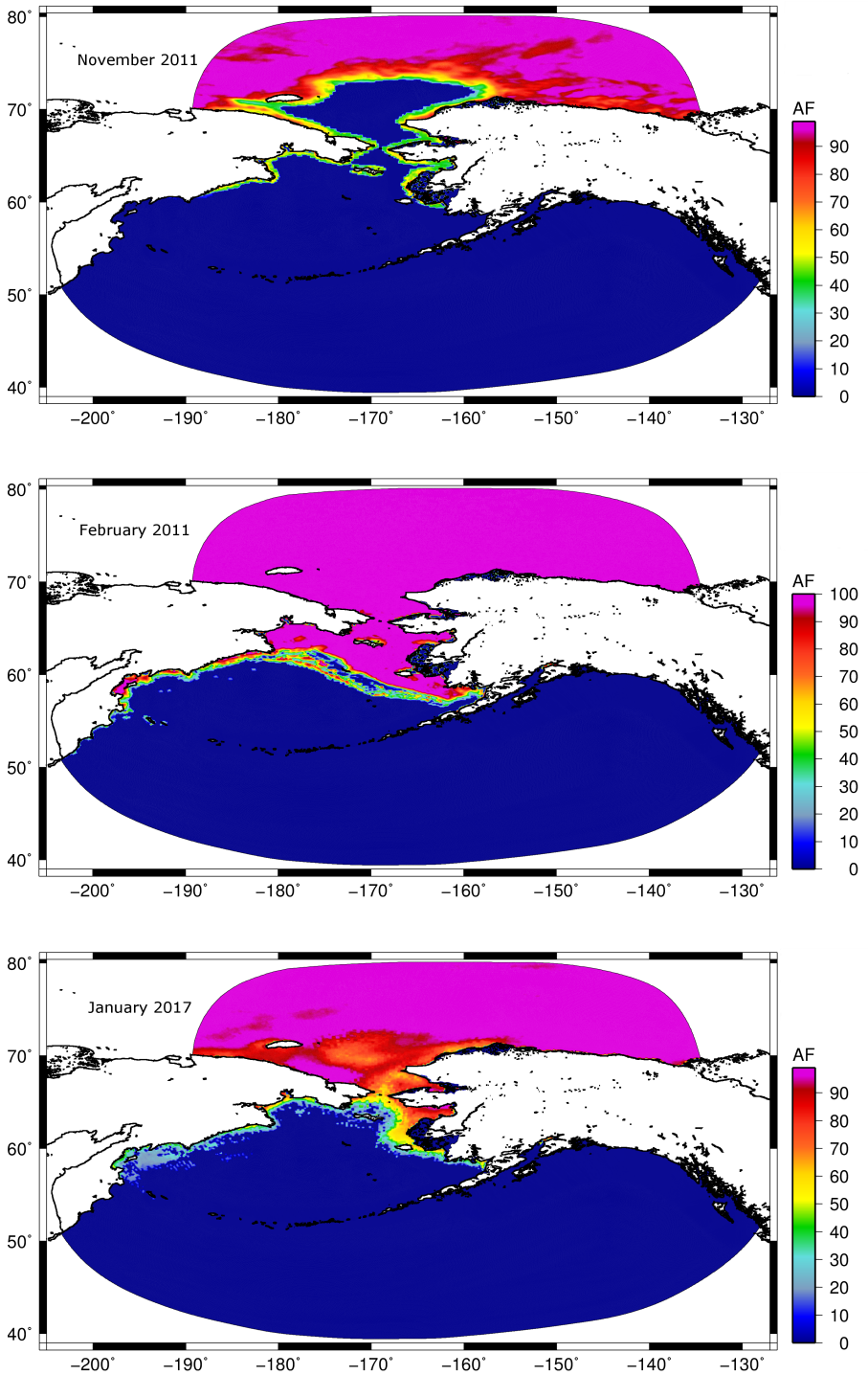

FIG. 16. Ice coverage (in terms of area fraction, AF) during November 2011 storm (November 7th, 2011 6:00 UTC), February 2011 storm (February 23rd, 2011 3:00 UTC), and January 2017 storm (January 1, 2017 0:00 UTC).

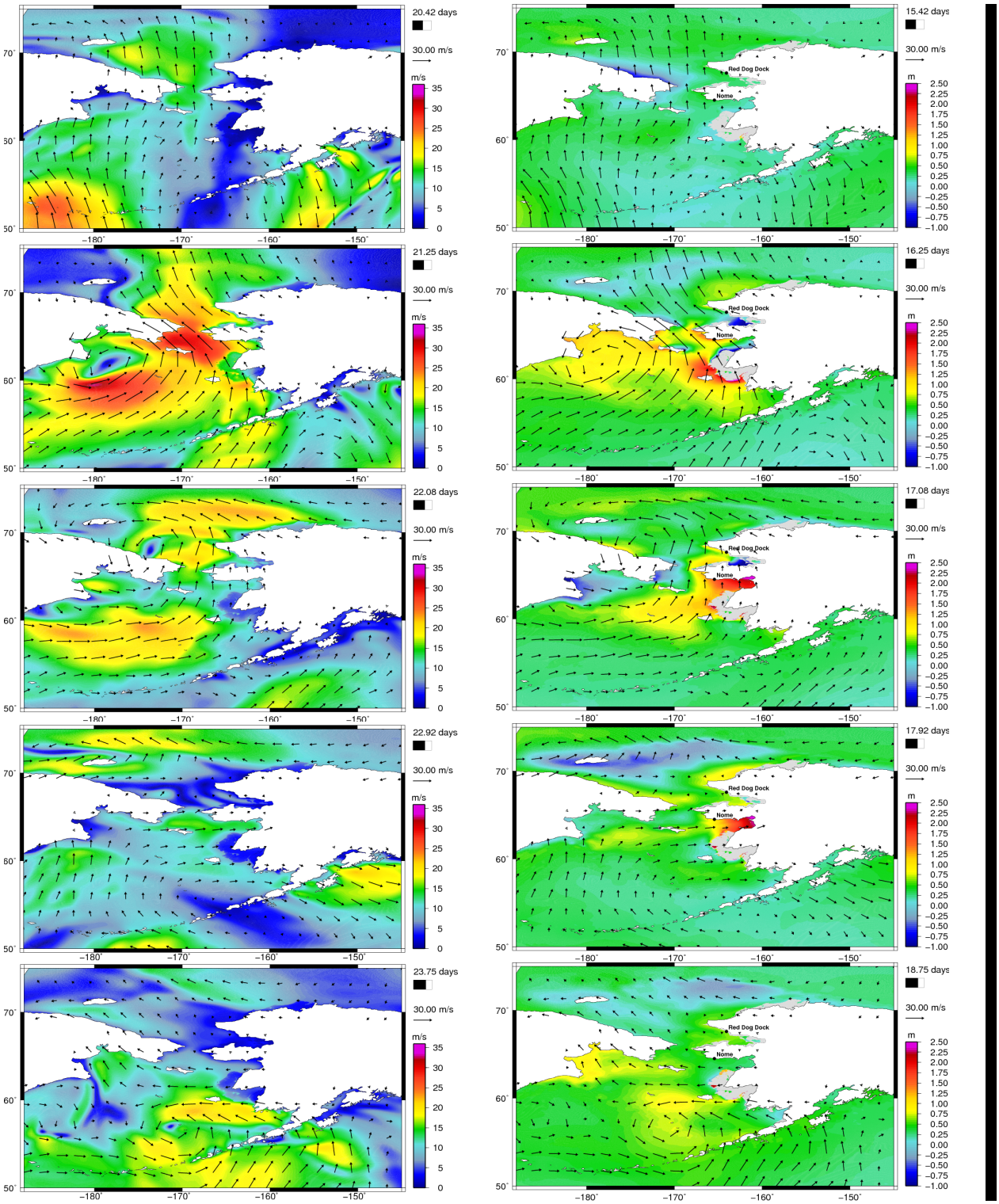

FIG. 17. Windspeed (left) and water surface elevation without tides (right) for the November 2011 storm. Fields shown are for November 8 10:00 UTC, November 9 6:00 UTC, November 10 2:00 UTC, November 10 22:00 UTC and November 11 18:00 UTC.

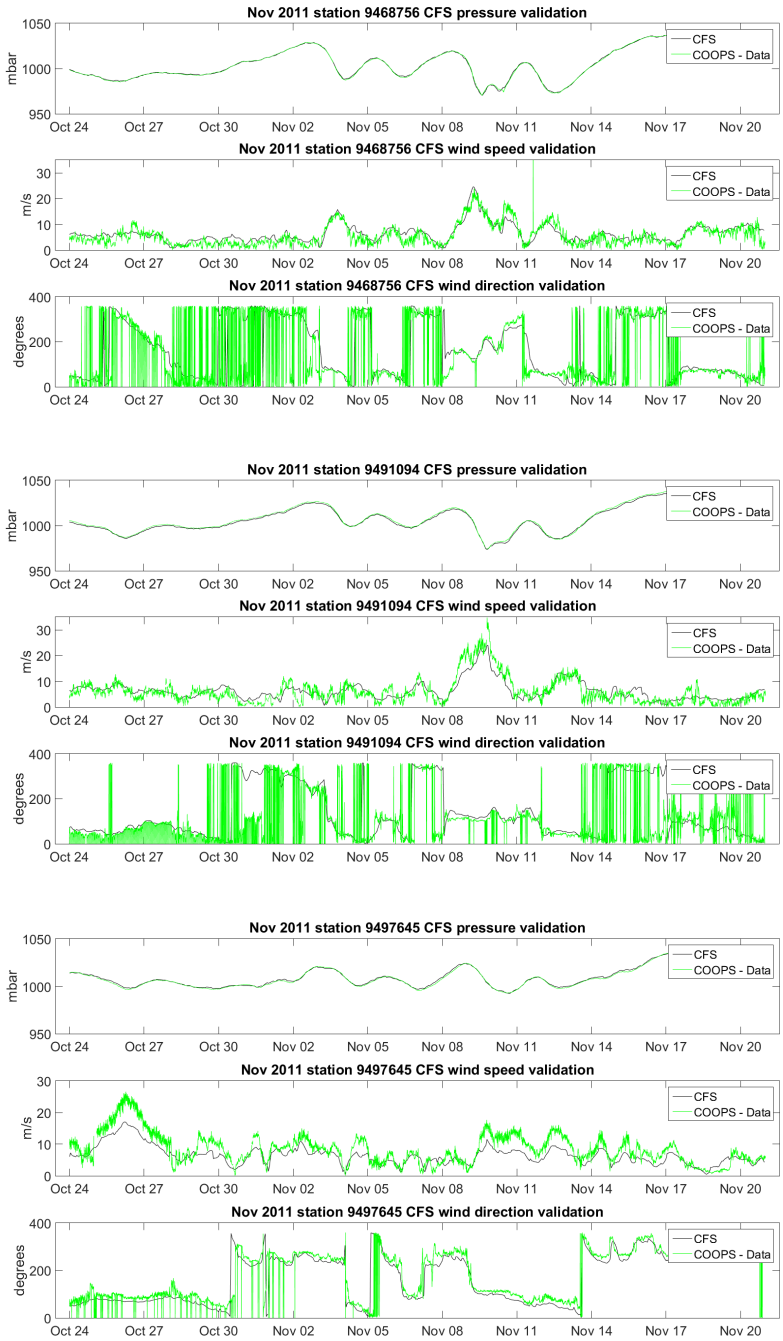

FIG. 18. Validation of CFSv2 pressure, windspeed and direction for November 2011 for Nome (9468756), Red Dog Dock (9491094) and Prudhoe Bay (9497645).

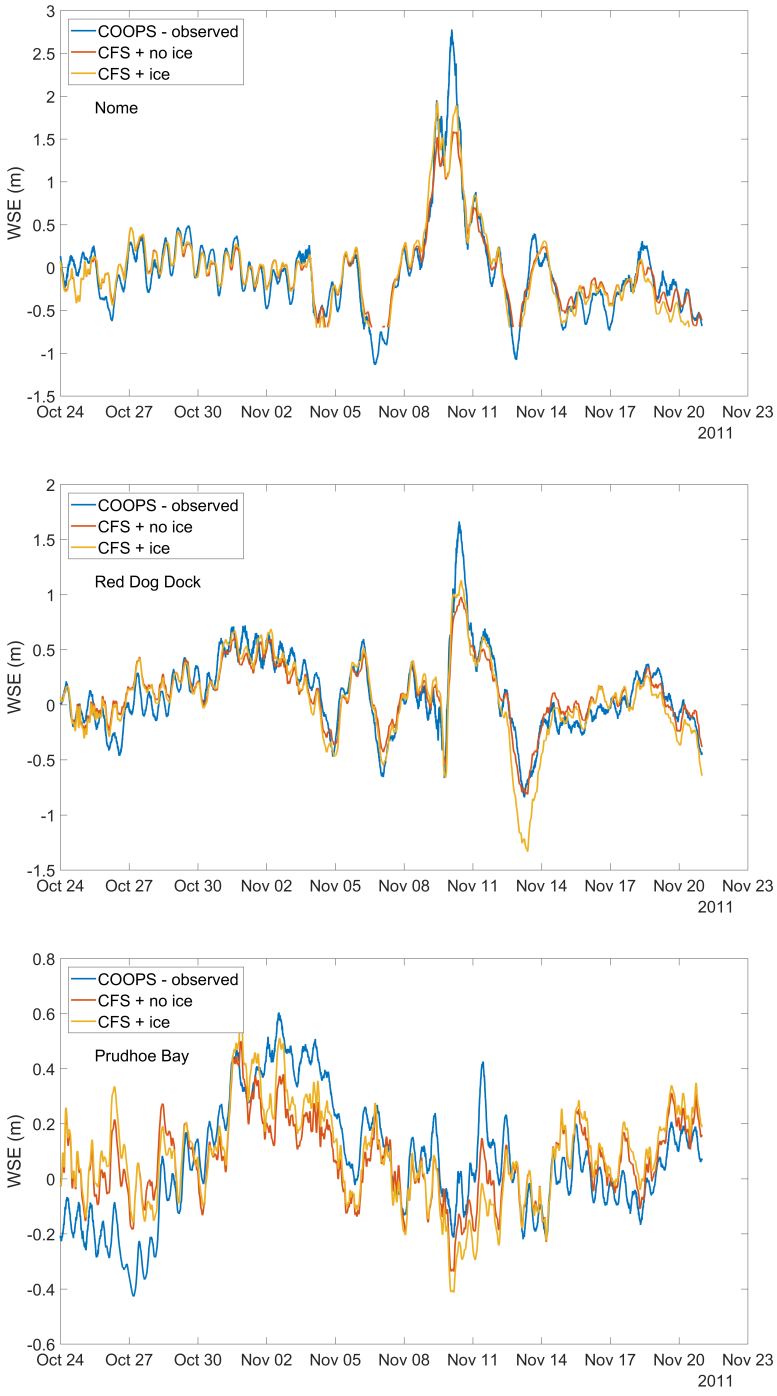

FIG. 19. Validation of water surface elevation as computed by ADCIRC for November 2011 for Nome (9468756), Red Dog Dock (9491094) and Prudhoe Bay (9497645) with (gold) and without ice (red).

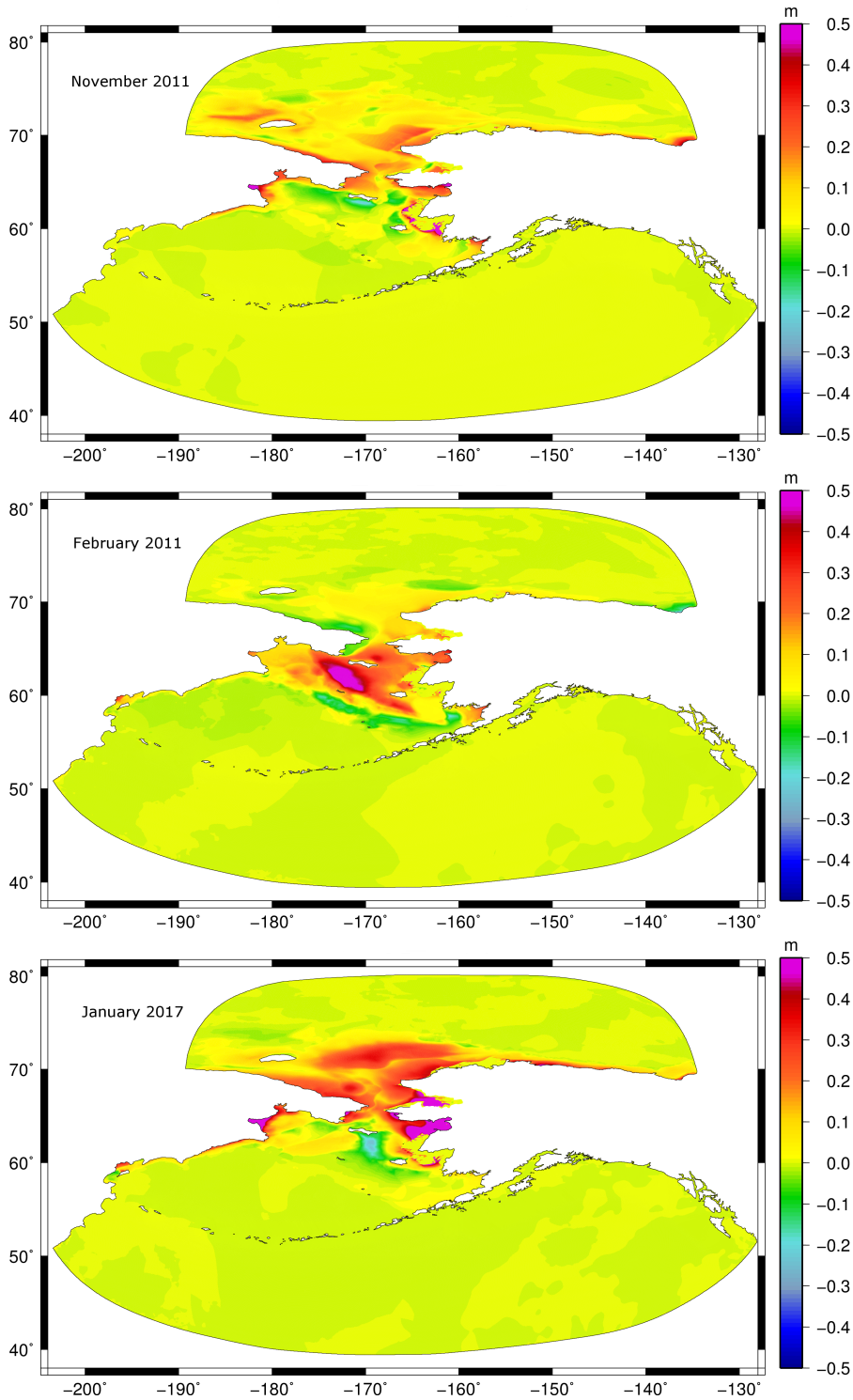

FIG. 20. Effect of sea ice on maximum modeled water surface elevation for November 2011, February 2011 and January 2017

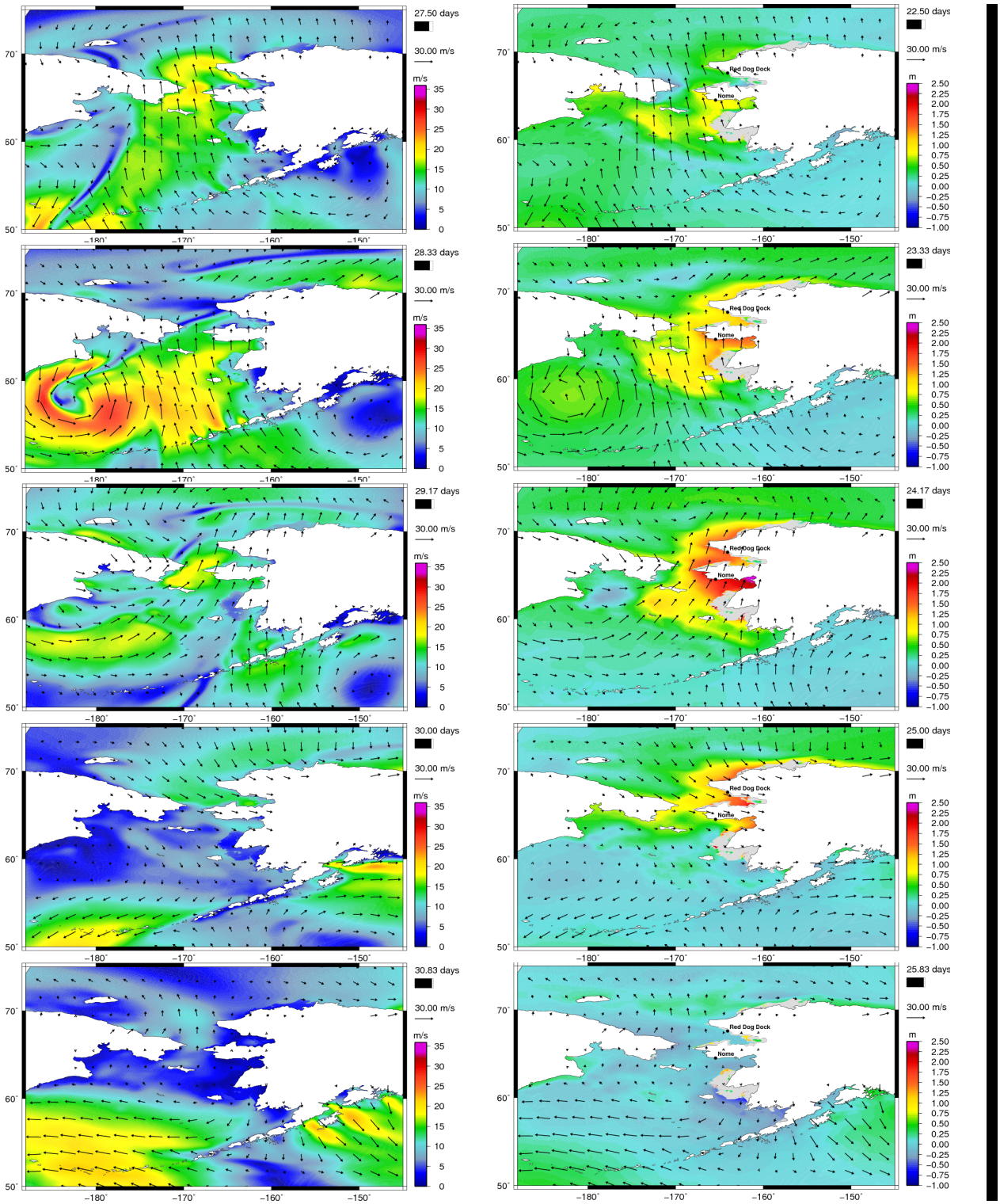

FIG. 21. Windspeed (left) and water surface elevation without tides (right) for the February 2011 storm. Fields shown are for February 22 12:00 UTC, February 23 8:00 UTC, February 24 4:00 UTC, February 25 0:00 UTC, and February 25 20:00 UTC.

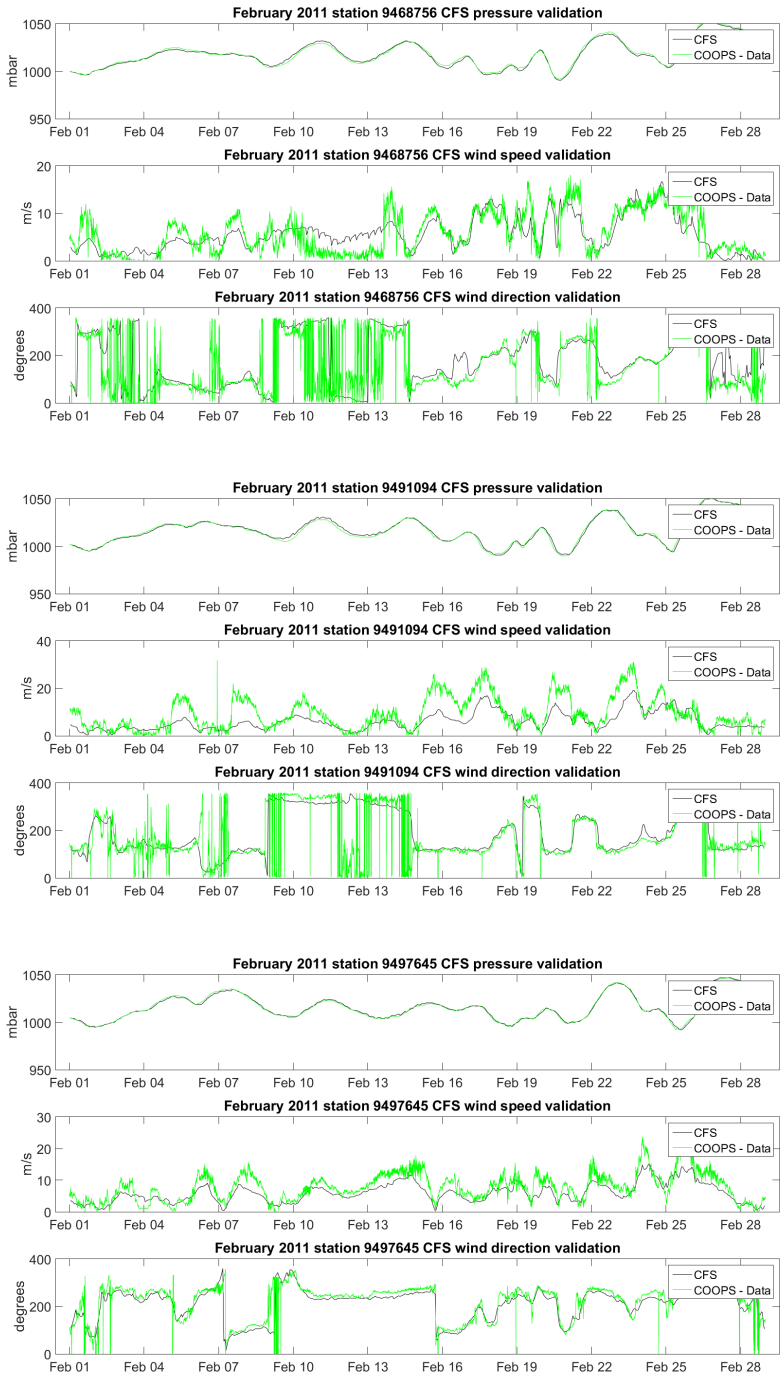

FIG. 22. Validation of CFSv2 pressure, windspeed and direction for February 2011 for Nome (9468756), Red Dog Dock (9491094) and Prudhoe Bay (9497645).

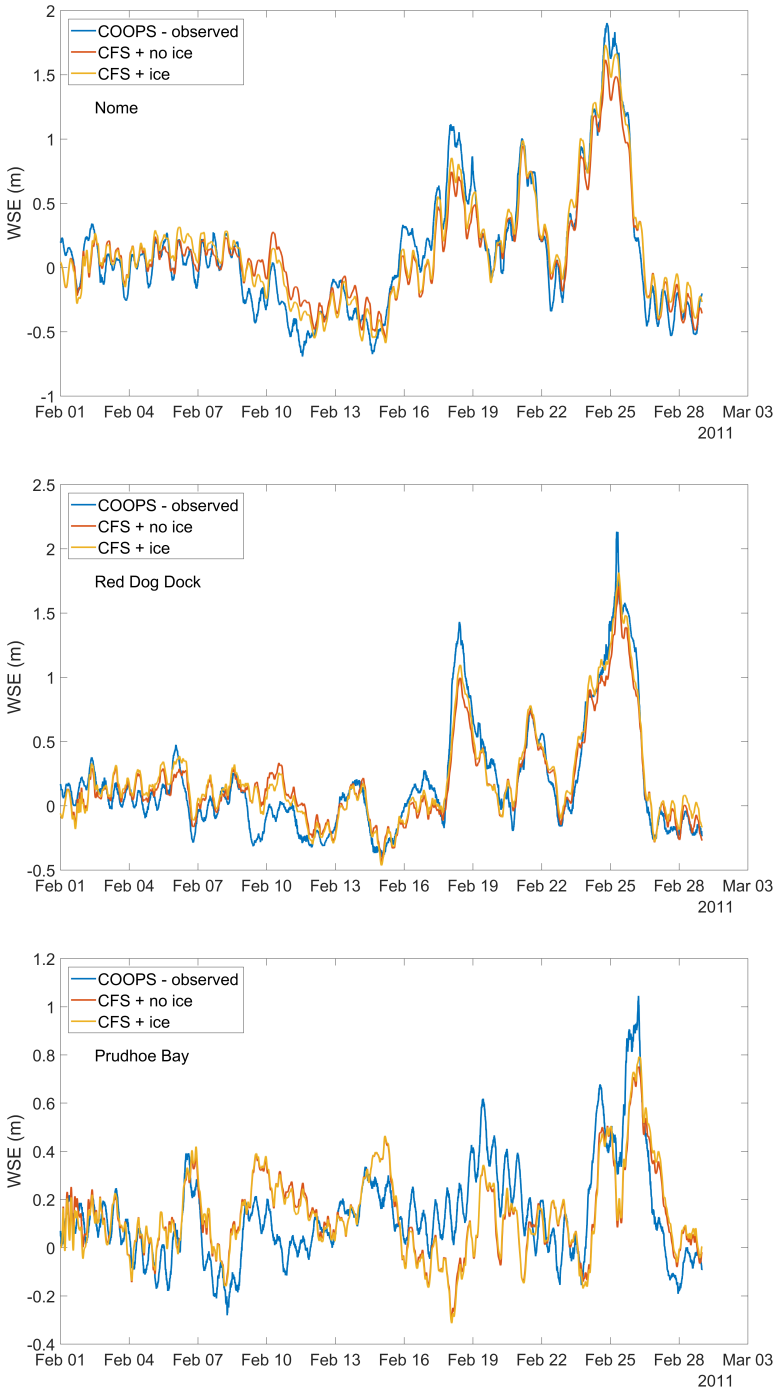

FIG. 23. Validation of water surface elevation as computed by ADCIRC for February 2011 for Nome (9468756), Red Dog Dock (9491094) and Prudhoe Bay (9497645), with (gold) and without ice (red).

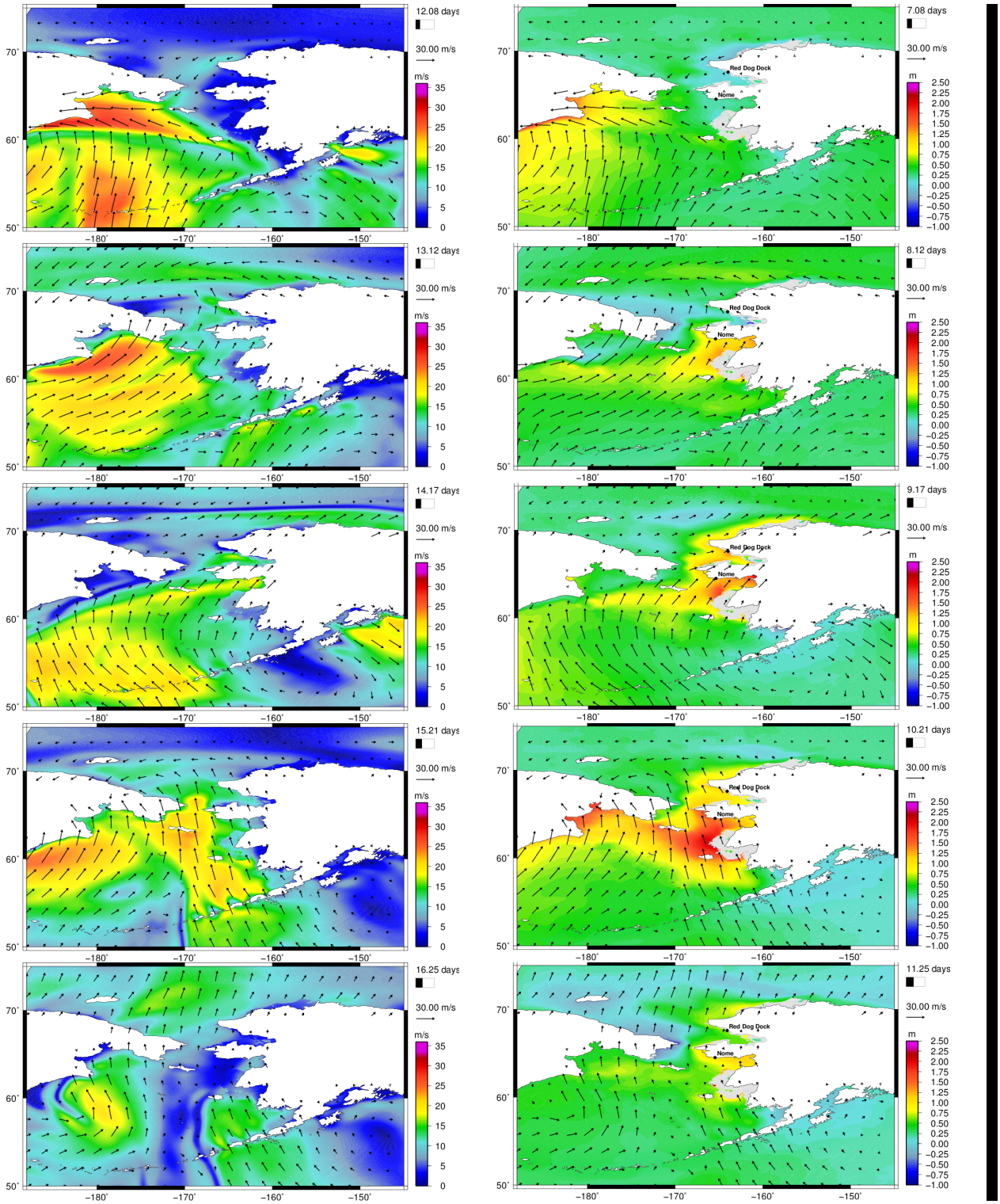

FIG. 24. Windspeed (left) and water surface elevation without tides (right) for the January 2017 storm. Fields shown are for December 29 2:00 UTC, December 30 3:00 UTC, December 31 4:00 UTC, January 1 5:00 UTC, and Janury 2 6:00 UTC.

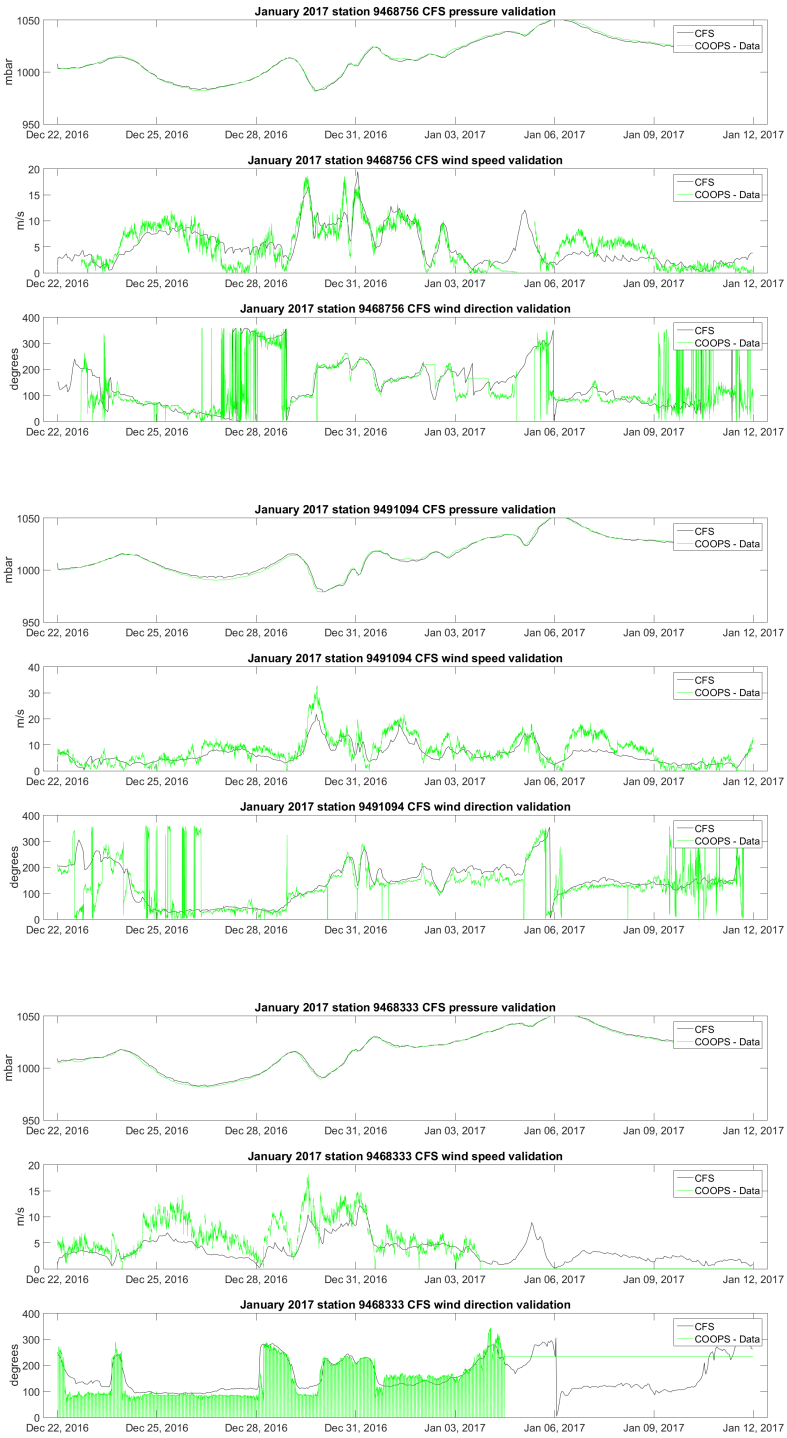

FIG. 25. Validation of CFSv2 pressure, windspeed and direction for February 2011 for Nome (9468756), Unalakleet (9468333) and Red Dog Dock (9491094). The Prudhoe Bay (9497645) meterological station was inactive during this event.

FIG. 26. Validation of water surface elevation as computed by ADCIRC for January 2017 for Nome (9468756), Unalakleet (9468333), Red Dog Dock (9491094) and Prudhoe Bay (9497645), with (gold) and without ice (red).